AFRL-RX-WP-TP-2011-4300

MICROSTRUCTURE EVOLUTION DURING FRICTION STIR WELDING OF MILL-ANNEALED Ti-6Al-4V (Preprint)

A.L. Pilchak

Processing Section
Metals Branch

J.C. Williams

The Ohio State University

W. Tang, H. Sahiner, and A. P. Reynolds

University of South Carolina

MAY 2011

AIR FORCE RESEARCH LABORATORY
MATERIALS AND MANUFACTURING DIRECTORATE
WRIGHT-PATTERSON AIR FORCE BASE, OH 45433-7750
AIR FORCE MATERIEL COMMAND
UNITED STATES AIR FORCE

REPORT DOCUMENTATION PAGE

Form Approved
OMB No. 0704-0188

1. REPORT DATE *(DD-MM-YY)*	2. REPORT TYPE	3. DATES COVERED *(From - To)*
May 2011	Journal Article Preprint	01 May 2011 – 01 May 2011

4. TITLE AND SUBTITLE
MICROSTRUCTURE EVOLUTION DURING FRICTION STIR WELDING OF MILL-ANNEALED Ti-6Al-4V (Preprint)

5a. CONTRACT NUMBER
In-House

5b. GRANT NUMBER

5c. PROGRAM ELEMENT NUMBER
62102F

6. AUTHOR(S)
A.L. Pilchak (Metals Branch, Processing Section (AFRL/RXLMP))
J.C. Williams (The Ohio State University)
W. Tang, H. Sahiner, and A. P. Reynolds (University of South Carolina)

5d. PROJECT NUMBER
4347

5e. TASK NUMBER
20

5f. WORK UNIT NUMBER
25100102

7. PERFORMING ORGANIZATION NAME(S) AND ADDRESS(ES)

Metals Branch, Processing Section (AFRL/RXLMP)
Materials and Manufacturing Directorate, Metals, Ceramics, and NDE Division
Air Force Research Laboratory
Wright-Patterson Air Force Base, OH 45433-7750
Air Force Materiel Command, United States Air Force

The Ohio State University

University of South Carolina

8. PERFORMING ORGANIZATION REPORT NUMBER
AFRL-RX-WP-TP-2011-4300

9. SPONSORING/MONITORING AGENCY NAME(S) AND ADDRESS(ES)

Air Force Research Laboratory
Materials and Manufacturing Directorate
Wright-Patterson Air Force Base, OH 45433-7750
Air Force Materiel Command
United States Air Force

10. SPONSORING/MONITORING AGENCY ACRONYM(S)
AFRL/RXLM

11. SPONSORING/MONITORING AGENCY REPORT NUMBER(S)
AFRL-RX-WP-TP-2011-4300

12. DISTRIBUTION/AVAILABILITY STATEMENT
Approved for public release; distribution unlimited.

13. SUPPLEMENTARY NOTES
PAO case number 88ABW-2010-3855, cleared 16 July 2010. The U.S. Government is joint author of this work and has the right to use, modify, reproduce, release, perform, display, or disclose the work. Submitted to Metallurgical and Materials Transactions A. Document contains color.

14. ABSTRACT
In this study, mill-annealed Ti-6Al-4V plates were successfully friction stir welded over a wide range of processing parameters using a tungsten – 1%La2O3 tool. Two K-type thermocouples embedded in the tool indicated that approximately 25 pct. of the heat generated during welding was transferred out of the workpiece and into the tool. The thermocouple data, combined with observations of the microstructure, indicated that the stir zone of all welds exceeded the β transus. The microstructure and texture of two representative welds made just above and high above the β transus were investigated with scanning electron microscopy and electron backscatter diffraction (EBSD). The β phase orientations were reconstructed with a fully automated technique from the as-collected α phase data through knowledge of the Burgers orientation relationship. The results suggest that the fine β grains in the stir zone are formed from the base material ahead of the advancing tool by dissolution of secondary and primary α phase and there is no further recrystallization.

15. SUBJECT TERMS
friction stir welding, stir zone, scanning electron microscopy

16. SECURITY CLASSIFICATION OF:			17. LIMITATION OF ABSTRACT:	18. NUMBER OF PAGES	19a. NAME OF RESPONSIBLE PERSON (Monitor)
a. REPORT	b. ABSTRACT	c. THIS PAGE			Donna Ballard
Unclassified	Unclassified	Unclassified	SAR	50	19b. TELEPHONE NUMBER *(Include Area Code)* N/A

Microstructure evolution during friction stir welding of mill-annealed Ti-6Al-4V

A.L. Pilchak[1,2,3], W. Tang[4], H. Sahiner[4], A. P. Reynolds[4] and J.C. Williams[1]

[1]The Ohio State University, Department of Materials Science and Engineering, The Ohio State University, Columbus, OH 43210

[2]Air Force Research Laboratory, Materials and Manufacturing Directorate, Wright Patterson Air Force Base, OH 45432

[3]Universal Technology Corporation, Dayton, OH 45433

[4]University of South Carolina, Department of Mechanical Engineering, Columbia, SC 29208

Abstract

In this study, mill-annealed Ti-6Al-4V plates were successfully friction stir welded over a wide range of processing parameters using a tungsten – 1%La_2O_3 tool. Two K-type thermocouples embedded in the tool indicated that approximately 25 pct. of the heat generated during welding was transferred out of the workpiece and into the tool. The thermocouple data, combined with observations of the microstructure, indicated that the stir zone of all welds exceeded the β transus. The microstructure and texture of two representative welds made just above and high above the β transus were investigated with scanning electron microscopy and electron backscatter diffraction (EBSD). The β phase orientations were reconstructed with a fully automated technique from the as-collected α phase data through knowledge of the Burgers orientation relationship. The results suggest that the fine β grains in the stir zone are formed from the base material ahead of the advancing tool by dissolution of secondary and primary α phase and there is no further recrystallization. These grains subsequently deform by slip and rotate towards the orientations that are most stable with respect to the shear deformation induced by the tool. In the highest temperature weld, diffusion tool wear in the form of periodically spaced bands provided an internal marker of the tool / workpiece interface during welding. The flow patterns evident within the tungsten-enriched bands suggest that flow is considerably more chaotic on the advancing side than in the central stir zone.

1. Introduction

Friction stir welding (FSW), invented in 1991 at The Welding Institute (TWI) [1], is a solid state joining process that has received significant attention throughout several industries because of its high success for joining aluminum alloys [2-4]. The process features a non-consumable rotating tool with a probe that is plunged into the seam between two sheets or plates to be joined. Local heating caused by friction between the rotating tool shoulder and the workpiece(s) reduces the flow stress of the material, and upon translation of the tool, the softened material is plastically deformed by the rotating pin [5]. Details of material flow during processing are generally difficult to measure experimentally and must be inferred from marker studies [6,7], the resultant stir zone microstructure and texture [8-14], and numerical simulation [15,16]. As depicted schematically in Figure 1, it is generally accepted that there is a layer of material, called the "shear zone" or "shear layer," that reaches the highest temperature and flows at the highest rate around the pin. This region also accumulates the highest amount of strain during welding and ultimately constitutes the stir zone after the tool has passed and deformation is complete. Outside of the shear zone is the transition zone [8] which serves as a buffer between the non-deformed material in the heat affected zone and the material moving at the highest rate in the shear zone. This region also experiences deformation during welding, but the total strains are smaller and the strain rates are lower than in the stir zone. Finally, the heat affected zone experiences a temperature rise during welding, but does not experience any strain due to the rotating tool.

Large scale EBSD analysis of friction stir welds has shown that the rotating pin imposes a state of simple shear that changes depending on the location around the tool where the shear direction is tangent to the tool rotational velocity and the shear plane normal is perpendicular to this tangent at any location [9,11,13,17]. This simple shear reference frame is illustrated schematically at four limiting locations around the tool in Figure 1. Cho and Dawson [15] have discussed how texture evolves in a smooth, organized fashion during friction stir welding by using the velocity gradients along stream lines of material flow determined by a finite element solution to drive lattice reorientation within a crystal plasticity framework. Their work showed how strain in the stir zone is accommodated by crystallographic slip and that the complicated deformation gradient imposed by the tool can be simplified into a combination of simple and pure shears between the limiting locations identified in Figure 1.

In titanium alloys, studies of the stir zone texture in near-α [13], α + β [18] and β [12] alloys have shown that the predominant texture components developed in the stir zone during welding above the β transus are consistent with those that are observed during simple shear deformation of body-centered-cubic (BCC) metals. Reynolds et al. [12] have observed a sharp simple shear texture in the stir zone of a metastable β alloy welded at a temperature above the β transus. Since metastable alloys do not undergo the β → α + β transformation upon cooling, the texture measured at room temperature was indicative of the texture at the deformation temperature. Mironov et al. [18] have also reported the β phase in Ti-6Al-4V exhibits a D2 simple shear texture during welding above the β transus. However, the authors noted that this was based on a limited number of measurements made within the narrow β ribs in the α colonies in the stir zone. Knipling and Fonda [13] have also noted that the α phase texture in the stir zone of near-α Ti-5111 mimics that of a BCC simple shear texture that has been transformed according to the Burgers orientation relationship.

Several studies have addressed aspects of microstructure evolution during FSW of Ti-6Al-4V [18-24], however the reported recrystallization mechanisms have been widely varying. For instance, some authors advocate dynamic recrystallization [21,22], although it is not specified whether it is a continuous or discontinuous process. Others have suggested that classical discontinuous recrystallization stimulated by local grain boundary migration is operative [24]. Mironov et al. [18,24] have described how elongated prior β grains might form during FSW above the β transus by transverse subdivision of existing β grains, but have not adequately described the base material (BM) condition. Another mechanism based on the formation of “bulges” from β grain boundaries was also described [24]. The examples for this mechanism were based on β grain boundary networks created from EBSD data in which boundaries that *did not* belong to one of the allowed angle/axis pairs for two variants inherited from the same prior β grain [25] were colored black. With this type of analysis, however, it is not possible to distinguish between the globular primary α and colony α + β (transformed β) known to be present in the TZ of Ti-6Al-4V friction stir welds made above the β transus [21,26,27]. Since the globular grains are formed through spherodization of an initially lamellar microstructure during large strain deformation [14], and not by classical nucleation and growth, they are not required to hold a specific orientation relationship with the adjacent β phase and thus could give rise to “false positives” using the reconstruction technique described above and could be responsible for the “bulges” described by Mironov et al. [24]. Thus, one purpose of the present work is to

clearly identify the mechanism, or mechanisms, which lead(s) to the formation of the fine prior β grains in the stir zone during welding above the β transus.

While there is disagreement about the precise grain refinement mechanism, it is generally agreed that it is a two part process characterized first by grain refinement followed by static coarsening of the as-deposited structure while it cools. Zhang et al. [22] have produced welds in a 3 mm thick Ti 6Al-4V sheet using a Mo-based tool and found that increased peak temperatures caused by higher tool rotation rates resulted in larger prior β grain sizes. Prior β grain sizes between 11 μm and 23 μm were measured from optical images for tool rotation rates between 300 rpm to 600 rpm, respectively, at a constant travel speed of 1 mm s^{-1}. Zhang et al. [22] have also noted an increase in the average prior β grain size with increasing tool rotation rate in 3 mm thick plates of Ti-6Al-4V. While these studies demonstrate a general trend in the β grain size, the effects of grain growth in the stir zone have not been separated from the initial grain size in the stir zone directly after welding.

One of the primary concerns regarding FSW of higher temperature materials like titanium is the welding tool. High temperature materials require the development of tool materials and geometries which will not suffer from significant wear and deformation under high temperature welding conditions [22,28,29]. For example, Pilchak et al. [14,30,31] have shown that sub-micron sized tungsten-rich particles are deposited in the stir zone during friction stir processing both above and below the β transus, although the degree of tool wear was greater during the latter due to the higher flow stress of the workpiece when α phase was present. Titanium alloys generally have a narrow window of processing parameters that produce suitable welds as compared to aluminum alloys. This is related to the low thermal conductivity of titanium alloys which is typically lower than that of the materials used to weld it. As a result, large temperature gradients can be created within the stir zone that can have an impact on process robustness [32]. Mechanistically, this is related to the fact that titanium alloys are quite susceptible to adiabatic heating caused by highly localized deformation which can lead to the formation of intense, localized shear bands of intense shear strain by an autocatalytic process. If the strain in the band exceeds the critical strain for ductile fracture, small voids can be formed on the slip band. Such voids are referred to as *strain induced porosity* in the literature [33] and have been observed during friction stir processing of Ti-6Al-4V [30].

In the current study, Ti-6Al-4V plates were welded using a W-1% La_2O_3 tool over a range of rotational and welding speeds. The process parameters used for each set of welds were correlated to feedback parameters including temperature, forces, torque, and power in order to gain a better understanding of the control parameter effects on process responses. In addition, temperatures were monitored at two locations in the tool during welding. The microstructure and texture of specimens was investigated with scanning electron microscopy and electron backscatter diffraction to assess microstructure evolution during processing. In particular, the formation of the fine prior β grains in the stir zone was tracked by first examining the BM followed by regions of the microstructure located progressively nearer the stir zone. These locations were judiciously selected to reflect regions that experienced increasingly higher peak temperature and total strain. The orientations and sizes of the β grains in each region were determined by employing a derivative of the automated reconstruction technique proposed by Glavicic et al. [34,35].

2. Materials and Experimental Procedures

The materials utilized for the present study were 10.3 mm thick Ti-6Al-4V plates in the mill-annealed condition. The welds were made for the purposes of microstructure evaluation, process response variable correlations, and to make in-tool temperature measurements. Bead on plate welds were made on the 10.3 mm thick plate using a W-1% La_2O_3 tool. A 25 mm diameter tool with a 9.9 mm long rounded probe was used. There were no flutes, threads or other reentrant features on the tool that would significantly alter material flow from the simple shear model described above.

The welding parameters utilized in this study have been summarized in Table I. Argon shielding gas was used to prevent oxidation of the weld surface and tool. Welding was performed under Z-axis position control. Position control welding was performed by controlling the plunge depth, which was initially set to the probe length for each weld. The depth was manually adjusted, when necessary, in increments of .025 mm to maintain adequate contact between the tool shoulder and the plate surface. The welds can be grouped into two series: one with increasing RPM and constant welding speed (50.8 mm/min) and another with constant advance per revolution (0.25 mm/rev) with rotation rate and welding speed varied proportionally (200, 400, and 800 rpm welds). The tool rotation direction was clockwise about the direction perpendicular to the welding plane.

Plan view and transverse cross sections were obtained from the welds using a combination of abrasive water jet and electrical discharge machining. Specimens for metallographic examination were prepared using progressively finer SiC paper and water through 1200 grit followed by polishing with 3 μm, and 1 μm diamond compound and a glycol-base extender. Final polishing was performed in a vibratory polisher using 0.05 μm non-crystallizing colloidal silica suspension. Heat tinting was used to reveal the microstructure of some specimens which were examined optically. The samples were heated to 600°C, held for 60 seconds and then removed from the furnace and allowed to cool to room temperature in still air. In addition, Kroll's reagent was used to etch samples for optical metallography. Specimens examined in the SEM were imaged in the as-polished condition using backscattered electrons.

In-tool temperature measurements were made using K-type thermocouples that were placed at two points along the centerline of the welding tool, as indicated in Figure 2, by spot welding the thermocouple into holes drilled in the tool. Thermocouple 1 (T1) was at shoulder level while thermocouple 2 (T2) was 12.7 mm above T1. A HOBO (Onset, Bourne, MA) data logger was used to record temperature measurements at a rate of 1 Hz during welding.

2.1 EBSD Analysis

Samples from the 2-200 and 8-800 welds were analyzed in detail. These welds were 25.4 cm and 45.7 cm long and the samples for analysis were cut 21.6 cm and 39.4 cm from the plunge point. These locations were chosen because they were well within the regime where the welding forces had reached nominally steady state conditions. Electron backscatter diffraction analysis was performed in an FEI XL30 ESEM equipped with a field emission source operated at an accelerating voltage of 20 kV and a probe current of approximately 2.5 nA. The as-polished specimens were positioned at a working distance of 21 mm at a stage tilt of 70°. Scans were acquired at step sizes between 0.35 μm and 1 μm on a hexagonal grid.

As mentioned above, there has been recent interest in studying the development of shear textures in the SZ as a means of understanding material flow patterns resulting from FSW of titanium. Due to the minimal amount of retained β, texture measurements from this phase were considered unreliable. However, because the α and β phases are related through the Burgers orientation relationship [36], it is possible to calculate the texture of the high temperature β phase based on the orientations of the inherited α variants. In this study, an automated method based on the equations of Glavicic et al. [34,35] was employed to

reconstruct the high temperature parent β grain orientations. Instead of using the global Monte Carlo minimization approach described in the original paper, we have used a nearest-neighbor approach to reconstruct the β grain structure [14,37]. In this method, each grain is assigned an integer and its orientation is represented as a quaternion in the sample reference frame. Each grain is interrogated, one at a time, and its orientation is compared to that of its neighbors to see if they satisfy one of the allowed misorientations for α variants inherited from the same prior β grain [25]. If the total number of α colonies that could have been inherited from the same prior β grain is greater than or equal to four [38], the six possible parent orientations are determined for the interrogated grain and its neighbors. The resulting orientations are compared and those which are the same within a user defined minimum misorientation angle (between 2.5 and 5^{o} here) are assigned that β orientation. The quaternion representation of orientation space is utilized, where an orientation is fully described by a single four-index vector, in order to implement a computationally efficient approach that minimizes the use of 'for-loops' in the array-based software language MATLAB® (The Mathworks, Inc., Natick, MA).

3. Results and Discussion

3.1 Temperature measurements

The results of the in-tool temperature measurements are shown in Figure 3. The profiles for all conditions were qualitatively similar with T1 temperatures that approached or exceeded the nominal β transus of Ti-6Al-4V (typically between 990 °C and 1000 °C for Ti-6Al-4V, depending on oxygen content [39]) for all welding conditions. None of the tool temperature measurements achieved true steady state conditions. Instead, the profiles all increased rapidly to a temperature near the β transus during plunging, followed by a gradual increase in temperature with increasing welding time. The T1 temperature in the 800 rpm exceeded the thermocouple limit (1304°C for K-type thermocouples), so the limit is shown. The time-temperature profile of the 150 rpm weld deviated slightly from that of the other welds in the sense that there was a more gradual approach to the near steady state temperature above the β transus. This profile was most likely due to insufficient initial shoulder contact that was corrected during welding by increasing the plunge depth.

The maximum T1 and T2 temperatures have been plotted with respect to tool rotational speed in Figure 4. Note that the welding speed for the 120, 150, and 200 rpm welds were equal while the welding speed was increased for the 400 (2x the 200 rpm welding speed) and 800 (4x the 200 rpm welding speed) rpm welds. The peak temperature measured on both thermocouples increased with increased tool rotation rate. The T1

temperature for the 800 rpm weld is based on a calculation (described subsequently) as the actual temperature exceeded the maximum temperature for the K-type thermocouple. This is indicated by the dashed line (rather than solid) in Figure 4 connecting the T1 800 rpm data point to the other T1 data points.

3.2 Process Response Variable Correlations

A steady state regime was determined for each weld based on the force profiles from which average welding forces were determined. A representative example from the 4-400 weld is shown in Figure 5. The x and y directions represent the force exerted by the plate on the tool in the translation and transverse directions, respectively, while the z-force acts along the tool rotation axis. The negative values of y force only represent the force direction. From these data, it is clear that the z-force became steady after about 50 mm welding, and it became unsteady again close to the end of the process, perhaps due to plate edge effects. The region between 50 mm to about 220 mm positions was considered as steady state in this weld. Average torque and welding forces were obtained for other welds in the same way.

The average welding forces were correlated with the rotational speed, as shown in Figure 6. As expected, the z-forces were highest among all of the welding forces for all weld parameters. The x-force (parallel and opposite to the welding direction) was higher than the y-force (perpendicular to welding direction pointing toward the advancing side) for the 120 weld, but was lower than the y-force at 150, 200, 400, and 800 rpm. The y-force was the least affected by process parameters, with a difference of 1.4 kN measured between the lowest (120 rpm) and highest (150 rpm and 400 rpm) averages. The high x- and z-forces at low rpm are most likely results of the comparatively low welding temperatures observed during welding. While the y-force was the least affected by weld parameters, it is clear that there was a significant decrease in x- and z-force with increased rotational speed at constant welding speed. However, when the welding speed was increased proportional to the rotational speed, no correlation can be made between the measured forces and processing parameters.

The average torque and welding power have been plotted against rotational speed in Figure 7. The average torque decreased with increased rotational speed while the average power increased with rotational speed. This result is consistent with observations made on aluminum alloys [40]. Lower torque is indicative of lower flow stress at elevated temperature. Process parameters appear to have a greater effect on the welding torque than on power at constant welding speed. This is evident in the steep gradients in the

torque / power – rotational speed plot (Figure 7). There was a large gradient from 120 rpm to 200 rpm on the torque correlation, while the power difference between the three welds was minimal.

Using the T1 and T2 temperature profiles, the heat flux through the tool was approximated assuming that conduction in the tool was 1-dimensional and steady state using the following equation:

$$q_{tool} = k\frac{\Delta T}{\Delta z} \quad (1)$$

Where q_{tool} is the heat flux in the tool in W/m-K, k is the thermal conductivity of the tool in W/m^2, ΔT is the difference in average near steady state welding temperature between T1 and T2, and Δz was the linear distance between thermocouples, 12.7 mm as shown in Figure 2. The thermal conductivity of the W-1%La_2O_3 tool was approximated using the elevated temperature thermal conductivity of pure tungsten, 110 W/m-K [41].

The heat flux was calculated for the 120, 150, 200, and 400 rpm welds and used in conjunction with the total welding power to determine what fraction of the total power could be accounted for by heat flux to the tool. Figure 8 shows that, on average, the heat flux accounted for ~25% of the weld power and this value was virtually independent of tool rotational speed. Based on this correlation, the peak temperature for the 800 rpm weld was estimated to be approximately 1550 ^{o}C. The dashed lines in Figure 8 indicate the estimated/assumed values for both heat flux as percent of power and the estimated maximum temperature for the 800 rpm weld. It is noteworthy that during FSW of aluminum alloys, heat loss to the tool as a percentage of heat generated is typically only about 5% [42]. This significant difference is related to the differences in the relative conductivities and thermal diffusivities of the tools and workpieces in aluminum and titanium friction stir welds. Aluminum has a greater conductivity and thermal diffusivity than the tool steels normally used for welding them, while, in contrast, the tungsten based alloy utilized in the present study has higher thermal conductivity than titanium.

3.3 Microstructure

The microstructure of each weld was qualitatively similar, with the stir zone being more or less “bowl” shaped and relatively featureless at the macroscopic scale with no bands or “onion” pattern evident. A representative cross section is shown in Figure 9. Four distinct regions can be identified in the cross section, namely, the SZ, TZ, HAZ and BM. The TZ and HAZ appear as dark and bright etching regions,

respectively. At this level of resolution, the BM also appears relatively featureless, however there is some evidence of preferential alignment of grains transverse to the welding direction. As mentioned, several studies have addressed aspects of microstructure evolution during FSW of Ti-6Al-4V [18,21,22,24], however, reports on the state of the BM are often limited. This is an important aspect to report, especially when the material is in the so-called “mill-annealed” state which has no specific meaning unto itself [39]. Therefore, in this section, we describe the state of the BM microstructure first, and then describe the evolution of each constituent at locations increasingly nearer to the tool. Due to the complicated initial condition of the BM, it was difficult to delineate clear borders between the heat affected, transition, and stir zones. There was, however, a continuous gradient in microstructure that, when considered in sequence, provides a clear indication of the path of microstructure evolution as material is first exposed to the thermal gradient ahead of the tool, then is swept around the tool and finally deposited in its wake.

3.3.1 Base material

A backscattered SEM image of the BM microstructure is shown in Figure 10a. The microstructure consists of globular primary α phase (α_P), acicular secondary α (α_S) and approximately 5 pct. retained β phase. The α phase is the darker phase while retained β is evident as bright regions due to the higher average atomic number. It is useful to recall the processing route which is used to create a mill-annealed structure in order to understand the state of the microstructure. Creating the mill-annealed condition is generally a three step process [39,43]. First, the alloy is homogenized in the β phase field. The time of this treatment will primarily influence the degree of homogenization and the underlying β grain size. After cooling, the workpiece is reheated and deformed at an elevated temperature in the α + β phase field. The strain in the workpiece is insufficient to fully recrystallize the microstructure resulting in the formation of the elongated primary α phase. This also implies that microtexture is formed, which is a phenomenon where large α colonies are not fully recrystallized during thermomechanical processing. This is not apparent from optical images, in which the grains appear equiaxed and recrystallized in the morphological sense, but EBSD studies have shown that regions of the microstructure consistent with the parent colony size have similar c-axis orientations [44,45]. Following deformation, the component is cooled, then heated again and partially stress relieved at a moderate temperature in the α + β phase field for the third step. This stress relief is typically for one to two hours between 650 ^{o}C to 700 ^{o}C and is insufficient to cause a significant change in the morphology or volume fraction of the constituent phases, although some thermally activated dislocation motion is inevitable [44].

The as-received material was characterized with EBSD by scanning an area of approximately 1.75 mm^2 that contained multiple microtextured regions at a coarse step size of 1 μm, and then performing a higher resolution scan at a step size of 0.25 μm on a smaller region. The former scan provided information about the macroscopic texture of the α phase while the latter, shown in Figure 11, provided an indication of the state of each constituent and also was able to capture the minority β phase constituent. The crystal orientation map in Figure 11a has been overlaid with a greyscale image quality map. The image quality parameter, calculated during EBSD data acquisition as a measure of pattern quality, provides a qualitative indication of the amount of stored energy in the lattice [44], although the image quality parameter is orientation dependent so one must be careful when interpreting this type of data.

An image quality map of a representative region of the BM microstructure, with boundaries between adjacent pixels colored according to their crystallographic misorientation angle, is shown in Figure 11b. There are α subgrains (α_{sub}) with misorientations ranging from 2^o to 15^o present between some of the recrystallized primary α grains (α_P). Other subtle orientation gradients (less than 2^o/0.25μm) were present in unrecrystallized regions of primary α. These regions were characterized by gradual changes in color (α_{unRX}, Figure 11a) and variations in image quality (Figure 11b) within individual deformed α grains. Subgrain boundaries and transgranular orientation gradients must physically be accommodated by geometrically necessary dislocations. Since neither the recrystallized primary α grains nor the transformed β regions (α_S) contained orientation gradients, it can be inferred that they had lower initial dislocation density than the unrecrystallized regions of the microstructure. This is consistent with partial recrystallization occurring during the mill-anneal [39]. It is noted, however, that the acicular secondary α (or transformed β) regions contain both low and high angle boundaries consistent with the crystallographic misorientations allowed for variants inherited from the same prior β grain [25]. Due to the differences in initial composition and dislocation density, each of these constituents will evolve differently during FSW and must be individually tracked through the HAZ, TZ and shear zone. In particular, due to their lower Al content, the α phase in the transformed β regions will tend to dissolve at much lower temperatures than the primary α phase. The underlying β grain size in the parent material microstructure can be inferred from the regions of similarly oriented retained β ribs shown in the crystal orientation map in Figure 11c. Three representative grains, between 5 μm and 25 μm, have been outlined in white.

The texture of the α phase in the base material is shown on 0001 and $10\bar{1}0$ pole figures in Figure 11d. The BM mainly exhibits transverse texture that is typical of α + β titanium alloys rolled high in the α + β phase field [39,46]. There is a weak basal component present (~2x), but the transverse component is much stronger (~13x). Peters and Lütjering [46] have shown that the ratio of the intensities of the basal and transverse components is a good indicator of the rolling temperature. Based on their results, we have estimated that the rolling temperature was between 960 ^{o}C and 980 ^{o}C for the present alloy. Within the welding reference frame defined in Figure 1, the tool travel direction during welding was transverse to the rolling direction such that there were many c-axes aligned with the welding direction. The β phase texture is also consistent with that expected during rolling of a BCC material. The texture, shown on 011 and 111 pole figures in Figure 11d, can be indexed specifically as the α-fiber of the BCC rolling texture [47,48].

3.3.2 Heat affected zone

The first change in microstructure observable with the SEM was an increase in the volume fraction of retained β phase. This was a gradual change because of the low peak temperatures reached in the far regions of the HAZ. This occurred first in the transformed β, manifested as a narrowing of the α lamellae, due to the lower Al concentration in these regions [39]. Nearer the stir zone, where the peak temperatures were higher, the α phase within the transformed β regions was completely converted to β phase at temperature and subsequently transformed back to α upon cooling (Figure 10b and Figure 10d) without any evidence of coarsening of the equiaxed α grains. The newly precipitated secondary α was quite fine indicative of a relatively fast cooling rate in this region. This is, however, nucleation and growth α as opposed to martensitic α'.

In Figure 10, there is also a noticeable difference in the relative contrast of the primary α and transformed β regions in the HAZ as compared to the BM. This is primarily due to the increased solubility of Al in the β phase with increasing temperature which lowers the average atomic number of these regions resulting in a darker appearance when imaged with backscattered electrons. This is also evidence for a moderately quick cooling rate because it this contrast difference is consistent with partitioning of Al and V to their respective phases being prohibited. This change was also gradual and continuous throughout the HAZ and into the TZ (Figure 10c). The border between these two regions was not clear because the dislocations already present in the elongated α in the BM could have become mobile due to thermal activation and continued the spherodization process that was started during the rolling operation. Thus, further refinement of the

elongated primary α bands would have been due to the temperature rise and not the deformation imposed by the tool. Thus, these regions should still be characterized as the heat affected zone [8].

3.3.3 Transition Zone / Shear Zone

In the transition zone, the peak temperatures were sufficiently high that the β phase was the majority constituent at the peak temperature but, there is still a measurable quantity of globular α phase remnant from the BM. A gradual decrease in the volume fraction of primary α through this zone was also observed until the microstructure consisted entirely of transformed β upon reaching the shear zone (Figure 1).

After the tool had passed, the regions of β phase transformed into a fine acicular α phase during cooling (Figure 10c). Due to the higher peak temperature here compared to the HAZ, the volume fraction of transformed β here was greater and also increased with decreasing distance from the stir zone. On the HAZ side of the TZ, grain boundary α was generally not observed in the transformed β regions indicating that no new β grain boundaries were formed, and thus the β phase was not recrystallized in this region. Contrast gradients within the globular α phase, which were not present in the as-received condition, however, confirm that this region had experienced deformation during welding. These contrast gradients are indicative of subgrain formation and arise from differences in the channeling behavior of the differently oriented hexagonal α phase subgrains. On the side of the TZ nearer to the SZ (Figure 12), however, fine β grains surrounded by grain boundary α were evident within the transformed β indicating that the β phase was either recrystallized, or that the volume fraction of β had increased sufficiently at the peak temperature that two differently oriented grains met forming a new β grain boundary. The new boundary gave rise to grain boundary α formation upon cooling from above the β transus. There was also significant subgrain formation within the globular α phase at this region.

Examinatinon of the β grain crystal orientation map in Figure 11c reveals that the latter mechanism is more likely since there are many adjacent transformed β regions which have significantly different orientation, although they all still along the α-fiber of the BCC rolling texture. In order to verify that this was the operative mechanism, EBSD maps were collected in the transition zone and shear zone progressively closer to the friction stir tool as shown schematically in Figure 1. Although the regions we have studied are on the advancing side, they are also representative of the state of the microstructure in the same regions ahead of, and in the direct path of, the tool. The primary difference is that material which enters the shear

zone ahead of the friction stir tool experiences additional straining as it is carried around the tool where it becomes part of the SZ once the tool has passed and it is no longer being deformed. On the other hand, material in the shear zone on the advancing side does not necessarily get carried around the tool and so it is representative of the state of the microstructure ahead of the tool just prior to being swept around the tool.

A partially reconstructed EBSD map from region A (Figure 1) is shown in Figure 13. The top of the figure shows the as-collected α orientations and beneath the horizontal black line is the reconstructed β phase, although some α remained untransformed as discussed in the caption. The texture of each phase (calculated from the as-collected and fully reconstructed maps) is shown to the right of the EBSD map in Figure 13. The β phase texture in this region is almost identical to that measured in the base material consisting of orientations distributed along the α-fiber of the BCC rolling texture. Bhattacharyya et al. [49] have shown with neutron diffraction that the β phase which forms during the α → β transformation upon heating inherits the existing β phase orientations, and strengthens its texture, as opposed to nucleating new β orientations by nucleation within the α phase. To be explicit, this would require that the β phase formed in the heat affected zone would inherit the BCC rolling texture which was indeed observed in the present case.

The persistence of the BCC rolling texture of the base material into the low-strained region of the TZ (very near the HAZ) suggests that the β phase was neither dynamically nor statically recrystallized in the HAZ or TZ as the tool passed. Instead, the β phase increased in volume fraction at the expense of the α phase in order to maintain phase equilibrium during the temperature rise. Due to the moderately quick cooling rate, the β phase transformed to α during cooling as opposed to growing epitaxially from the equiaxed α grains. While the data in Figure 13 demonstrates this point adequately, it is worth mentioning that the automated reconstruction technique cannot distinguish between primary α and the acicular α phase contained within the transformed β. Furthermore, the elongated (and spherodized) α is not necessarily related to the β phase through Burgers orientation relationship which could result in improperly calculated β grain orientations. Thus, three higher resolution scans (0.35 μm step size), 75 μm x 75 μm each, were acquired and analyzed interactively so that the β grain orientations were calculated only from the individual packets of transformed β that were selected by the user. Careful interactive analysis confirmed that the orientations of the β grains in the transformed β regions in the TZ in the high resolution scans (designated by numbers 1

through 3 in Figure 1) were consistent with those calculated by the automated reconstruction process (Figure 13).

We recognize that the α-fiber from the rolling reference frame is related to the {110}<uvw> partial fiber in the simple shear reference frame by a 90° rotation about the rolling sheet normal direction (or, alternatively, 90° about the tool rotation axis opposite to the tool rotation direction) [50,51]. The two textures are thus indistinguishable from one another on the advancing and retreating sides and it is tempting to relate the calculated texture to the simple shear deformation induced by the tool. However, examination of the α and β phase morphology in this region does not reveal features consistent with simple shear induced deformation. For instance, neither the remnant α phase constituents nor the β grains are elongated in the direction of simple shear which is typical for regions of the TZ affected by the shear induced by the rotating tool [8,14,20,18].

Due to the (α + β) → β → (α + β) phase transformation sequence that occurred in the TZ, the α phase texture in this region is different than that in the BM. Since the β phase was not recrystallized, it retained the BCC rolling texture and thus the α which formed from it only has a limited number of {110} planes and <111> directions to choose from in order to satisfy the Burgers orientation relationship. Review of the as-received material texture (Figure 11d) revealed that there were very few 0001 poles parallel with the rolling direction, however, after the phase transformation sequence, there is a significant [0001] || RD component evident that is almost as strong as the transverse basal component (Figure 11d). This type of preferential phase transformation is commonly known as variant selection [52] and is caused by the anisotropy in the transformation strains associated with the BCC to HCP phase transformation or due to dislocation activity on {110} planes in the β phase [44,53]. In Figure 11d, it is evident that the highest density of {110} planes lie in the shear plane putting them in an orientation favorable for slip. The observed α phase texture is consistent with {110}<111> slip occurring in the shear plane which biased the β → α phase transformation, however, the long range elastic stress field induced at this location in the plate is unknown and the possibility of its influence cannot be ruled out.

3.3.4 Stir Zone

The stir zone microstructure of all the welds was similar consisting of prior β grains, decorated by grain boundary α. A typical backscattered electron image of the stir zone microstructure, taken from the 200 rpm

weld, is shown in Figure 14. There were with multiple α variants present inside the prior β grains which formed an interpenetrating basket-weave microstructure. The prior β grain size increased with increasing tool rotation speed. The average prior β grain size was estimated by the linear intercept method from optical images made at the center line of the weld on transverse cross sections. The low rpm welds, made at 120 rpm, 150 rpm and 200 rpm, exhibited prior β grain sizes of 15 μm, 18 μm and 21 μm, respectively. The welds made at 400 rpm and 800 rpm exhibited average grain sizes of 53 μm and 80 μm, respectively. This can be rationalized on the basis that higher tool rotation rates led to increased peak temperatures reached in the stir zone and thus there was more time for β grain growth above the β transus after the tool had passed.

In the 800 rpm weld, which reached the highest peak temperature, a banded structure (Figure 15) that is similar to the banded structures commonly observed in aluminum alloy friction stir welds, was observed. Banding in Al alloys has been related to spatial variations in grain size, the distribution of second phase particles [54] and variations in simple shear texture components [55]. However, in the present study, energy dispersive spectroscopy revealed that the band contrast was due to the presence of tungsten in solid solution leading to local elevation of the average atomic number. In addition to the W in solid solution, discrete pieces of W-containing tool material (Figure 16a) were observed. The bands began at approximately the central stir zone and extended to the advancing side where they all joined and formed one narrow line corresponding to the periphery of the pin. On average, the band spacing was slightly larger than the tool advance per revolution, which was 254 μm rev^{-1}, although the spacing measurements were complicated by the width of the bands, over 100 μm wide in some cases. The spacing of these bands was also approximately consistent with the spacing of the grooves left on the surface of the plate behind the tool.

Tungsten is a β eutectoid forming element with titanium and is completely miscible within the β phase, but has extremely low solid solubility in α phase [56]. It is also a heavy, slow diffusing element that tends to retard phase transformation and growth kinetics. This is evident by comparing Figure 16b and Figure 16c which show the morphology of the α laths outside and inside the W-enriched bands, respectively. The α phase have higher aspect ratio and are considerably more narrow when W is present. Two discrete particles of the tool that were worn off that are not located within the bands are shown in Figure 16b. The bright halos around the W-rich particles represent the furthest that W could diffuse during the elevated

temperature excursion after the tool had passed, approximately 3 μm. Thus, it must be concluded that the bands were not formed by wear of discrete chunks of tool material followed by diffusion. The formation of this structure is more likely due to *diffusion wear*, which is a phenomenon known to occur during high speed machining of Ti-6Al-4V alloys when using tungsten-carbide tools [57]. This observation proves unequivocally that there is no localized melting at the tool/material interface in the welds made in this study, since all of the other welds were made at lower peak temperatures. It is likely that this observation holds for other titanium FSW processes as well since the tool rotation rate used for this weld (800 rpm), which has been demonstrated to be the strongest processing parameter that influences peak stir zone temperature, are much higher than those typically reported for FSW Ti-6Al-4V in the literature [18,20-23]. Of course, however, differences in tool size and geometry could lead to variations in the temperature in and around the FS tool.

The bands were wider near the central stir zone, where the tool travel velocity and the rotational velocity are orthogonal, than they were on the advancing side where these two velocities were parallel. In the lower magnification images of the bands (Figure 15, Figure 16a, and Figure 17), the contrast differences associated with the titanium-rich and tungsten-rich regions within the bands provides a qualitative indication of material flow behavior directly at the tool / workpiece interface. On the advancing side (Figure 17), the contrast gradients indicate significantly more chaotic flow patterns with folds and kinks that result in material apparently traveling backwards in some locations. These features may be evidence for the occurrence of the “slip-stick” phenomenon that has been described to occur at the tool / workpiece interface in the literature for aluminum alloys [6].

If tool wear is indeed due to diffusion of W, the periodic spacing of the bands suggests that they are caused by a period buildup / dissipation of heat at the tool / workpiece interface. Since titanium has a lower thermal conductivity than the tool material, the buildup of heat occurs on the titanium side. Diffusion occurs preferentially at this “hot zone” which progressively cools as the lower temperature tool material diffuses into the β Ti until the steady-state processing temperature is reached and the process begins again. The structure within the bands differed significantly from that outside. There were defects observed at some of the prior β grain boundaries within the bands, such as that shown in Figure 16d. The area enclosed in the dashed box corresponds to the particles as imaged with secondary electrons using the through-lens-detector. In this high resolution mode, and after various stage tilting experiments, it was determined that

there were a combination of non-conductive particles, voids and W particles at the grain boundaries. The non-conductive particles were most likely based around La_2O_3. In addition to the voids, some prior β grain boundaries within the bands showed signs of severe plastic deformation as opposed to smooth curvature, like those β grains between the bands, consistent with interfacial energy driven boundary migration. One example of this is shown in Figure 16c in which serrated and kinked grain boundary α features are evident. The implications of the voids and deformed grain boundaries is that the prior β grain structure present within the bands that are observable at room temperature are the same grains that were present at high temperature during welding. This is physically possible because of the retarding effects of W; there was not enough time at temperature for significant coarsening after the tool had passed and deformation had ceased for diffusional processes to occur.

Having established these grains were present at high temperature, it becomes significant that they are similar in size to those observed to form by dissolution of α phase within the HAZ, TZ and shear zone as they are swept into the material flowing at high rate around the tool. This implies that those grains formed naturally from the BM are not necessarily further refined as they are swept around the friction stir tool. From a deformation processing perspective, it is plausible that the grains developed ahead of the tool from the initial microstructure can react to the deformation imposed by the tool by crystallographic slip without the need for further grain refinement or to invoke a recrystallization mechanism. Assuming this is true, the β phase should exhibit a deformation texture that reflects the shear induced by the rotating tool. Additionally, the prior β grain size should vary spatially, and proportionally, with the different peak temperatures reached in the stir zone due to the different times available for grain growth.

In order to investigate these phenomena, we have calculated the texture of the β phase and the prior β grain size distributions from reconstructed EBSD data acquired at all of the locations shown in Figure 1 in the 800 rpm weld, and also from locations C and D in the 200 rpm weld. The β phase texture was analyzed and interpreted with respect to the simple shear reference frame imposed by the tool at locations B, C and D in the 800 rpm weld (locations C and D only in the 200 rpm weld). In the 800 rpm weld, the location of scan D corresponded to a region of the SZ between two W-rich bands.

Representative data from the central stir zone and advancing side of the 800 rpm weld are shown in Figure 18 and Figure 19, respectively. These figures show the α phase orientations measured in each location, the

β orientations reconstructed from it, and the texture of each phase. Similar figures were created for all locations analyzed, but due their similarity with those presented, the others have been omitted. It is noteworthy that in the 800 rpm weld that the bright, vertical line on the advancing side (Figure 17) created by tool wear at the periphery of the pin corresponds to the interface between the stir zone and shear zone as illustrated schematically by the dashed line in Figure 1. The microstructure on either side of this interface would otherwise be indistinguishable if not for the bands and so this location was only directly observable in the 800 rpm weld and, to our knowledge, for the first time ever in any friction stir welded material. An image quality overlay has been used on the EBSD maps in Figure 19 to emphasize the location bands in the image.

In the central stir zone (Figure 18), the β phase texture in the central stir zone coincides exactly with that expected in this location according to the Figure 1. The β phase texture consisted of orientations along the characteristic {hkl}<111> BCC simple shear partial fiber, most notably the E1 and E2 components, as compared to the {110}<uvw> partial fiber texture present in the BM. The α phase texture in this region was of moderate strength, 6x random, with 0001 poles being spread approximately equally over the 011 poles of the BCC shear texture indicating there was no strong variant selection. In contrast, on the advancing side (Figure 19), the strongest intensity on the 011 pole figure corresponds to the strongest intensity on the 0001 pole figure and both are approximately twice that of all the others. This pole is oriented ~70^{o} from the tool rotation axis and corresponds to the E1 component of the BCC simple shear texture, if one were to assume the strongest 111 poles were aligned with the shear direction. The remaining intensities can then be indexed as D1/D2 or E2 components. Perhaps the most striking feature on the advancing side is the considerable deviation of the β phase texture from that of the presumed simple shear reference frame imposed by the rotating tool (Figure 19). While the β phase still exhibits the characteristics of a shear texture, the shear direction implied by the texture is rotated 26.5^{o} about the tool rotation axis (opposite the direction of tool rotation) from its expected position (as depicted in Figure 1). The deviation here may be related to unsteady flow at the tool / workpiece interface, or the fact that the simple shear reference frame does not account for the effect of the tool translational speed, which was high in the 800 rpm weld (203.2 mm min^{-1} or 3.39 mm s^{-1}) in order to maintain constant tool advance per revolution. However, because of the high strain rates during welding, it is also possible that the deformation gradient that sets up the texture on the advancing side is imposed while the material is still being carried around the back of the FS tool towards the advancing side where it is eventually deposited. It is possible that one might use this deviation

to estimate the local strains using crystal plasticity formulations [48], however this is beyond the scope of the present study.

In order to further investigate this result, additional EBSD data was collected from a region of material in the shear zone (location B, Figure 1), just slightly further from the tool than the advancing side location described above. While the corresponding EBSD map is not shown, the α and β phase textures calculated from it are shown in Figure 20. The pole figures reveal a similar deviation, however the magnitude is approximately half of that measured at location C. Just slightly further from this position (transition zone, Figure 13), as already discussed, the texture was more consistent with that of the base material. In the central stir zone and on the advancing side, the β phase texture consisted of distinct components on the {hkl}<111> partial fiber as opposed to being spread over the {110} partial fiber as they were in the BM and TZ. These observations are consistent with the grains in the central stir zone and advancing side experiencing larger strains than those in the TZ. Baczysnki and Jonas [50] have discussed how the D and E simple shear texture components are more important with regard to texture evolution at elevated temperature, which may help explain their formation within the SZ. In addition, the authors have also discussed deviations from ideal textures on the basis of the orientation stability and the convergence-divergence field of BCC crystals subjected to simple shear. They found that at low strains, the deviation is generally opposite the applied shear direction whereas at large strains ($\varepsilon > 4$), the tilt tended towards the shear direction. We have assumed that large strains have accumulated within the stir zone, and therefore, cannot attribute the deviation of the texture to this mechanism since it opposes the shear direction. Additional work is needed to understand this phenomenon.

Similar EBSD analysis and automated reconstruction of the parent grain orientations was also performed in the central SZ and advancing side of the 200 rpm weld. The orientation maps have been omitted, but the measured α phase and calculated β phase textures from these data are shown in Figure 21. The texture in both locations is considerably more diffuse than the corresponding regions in the 800 rpm weld, although the characteristics of the textures are similar. For instance, the 111 poles are preferentially aligned with the shear direction in the central SZ, but not on the advancing side. The 200 rpm weld also exhibited an increased propensity for variant selection on the advancing side. While more diffuse than the 800 rpm weld, the simple shear characteristics could still be identified in the β phase texture on the advancing side and in the central stir zone. In the latter, the β orientations were distributed along the {uvw}<111> partial fiber with

some preference for clustering around the D1/D2 and E1/E2 orientations. The deviations from the ideal textures in these regions can most likely be attributed to difficulties in precisely identifying each location in the microscope since there were no W-enriched bands to use as an internal marker like in the 800 rpm weld.

The grain size distributions in Figure 22 confirm that the average β grain size increases with increasing peak temperature. In the 800 rpm weld, the smallest β grains were observed in the transition zone, where there was some untransformed α phase present, which inhibits β grain growth. These grain sizes are all comparable to those in the base material microstructure, as inferred from the β phase EBSD data in Figure 11c. The advancing side and central stir zone distributions in the 200 rpm weld revealed average grain sizes slightly larger than those in the TZ of the 800 rpm weld, suggesting that the time at elevated temperature in this weld was relatively short. Of these regions in the 200 rpm weld, the distribution for the central stir zone shows a slight increase in the number of larger β grains. This bi-modal distribution becomes more evident in the shear zone, advancing side and central stir zone of the 800 rpm weld. There was considerably more time for grain growth in these locations which show a gradual increase in the fraction of large grains compared to small ones at each location, respectively, consistent with increasing peak temperature. These observations are all consistent with growth of the larger population of grains at the expense of the smaller ones.

The mechanism of β grain formation described here is quite different from the dynamic recrystallization [21,22], discontinuous recrystallization [24] or transverse subdivision [24] mechanisms that have been previously proposed. The results of the present study suggest that neither dynamic nor discontinuous recrystallization is operative. Instead, it appears that fine β grains are formed from the initial microstructure in the thermal gradient ahead of the tool. As the tool approaches, these grains begin to deform with their straining direction dictated by their location around the FS tool. The β grains deform by crystallographic slip and rotate towards orientations on the ideal simple shear fibers. The material can deform by easy glide to accommodate the evolving simple shear reference frame as it is carried around the tool. The present results cannot entirely rule out the mechanism of transverse subdivision of existing prior β grains. However, it is likely that the contribution of this mechanism would be extremely limited in mill-annealed materials which start with small prior β grain size, but might be more important for coarse grained cast alloys where the large β grain size would need to be broken down in order to be amenable to the high rate deformation

that occurs in the shear zone, for example. The β grain formation mechanism we have described can adequately explain a range of experimental observations commonly reported during FSW of titanium alloys. Namely, the presence of elongated prior β grain morphology [18,20], fine prior β grain size [21-23] and the presence of shear textures [12,13,18] in the SZ. Finally, it is worth mentioning that although a steady state temperature profile was never achieved in the present study, the mechanism of β grain formation would not be expected to vary along the length of the weld because ultimately all of the α is dissolved leaving β grains which enter the SZ. This statement is strengthened by the fact that the mechanism of β grain formation was the same in the 2-200 and 8-800 welds which had significantly different temperature profiles.

4. Summary and Conclusions

In this study, friction stir welds were made in a 10.3 mm thick Ti-6Al-4V sheet using a W-1% La_2O_3 tool. The tool temperature was measured at two points in the tool during the welding process. Tool temperature increased with increasing rpm and weld power input. Temperature measurements and microstructure evaluations indicate that for the welding conditions used, the maximum temperature of the material in the stir zone was above the β transus. Analysis of the heat flux to the tool indicates that approximately 25% of the heat generated is transferred out of the workpiece and into the tool. This is in contrast to most calculations for steel tools and aluminum workpieces which indicate approximately 5% heat loss to the tool. Parameter correlations with feedback response data indicated a decrease in torque, x-, and z-force with increased rotational speed at a constant welding speed. The torque further decreased when the rotational speed and welding speed were increased by identical factors. The weld power increased with increased rotational and/or welding speed. The weld parameters had little effect on the y-force.

The microstructure in the stir zone consisted of fine, interpenetrating α platelets and small α colonies. EBSD analysis and automated reconstruction of the parent β grain orientations in the TZ, shear zone and stir zone revealed a clear path of microstructure evolution beginning with complete characterization of the base material. The β grains were formed initially from the transformed β regions in the base material which grew in size due to higher peak temperatures reached in the HAZ , TZ and shear zone until new β/β grain boundaries were formed. Since the initial β grain size was small, these grains were amenable to high rate deformation without further recrystallization. The β grains were then carried around the FS tool, dictated by the local simple shear reference frame, and deposited in its wake where they coarsened during cooling.

The amount of coarsening depended on the peak welding temperature which dictated the time available above the β transus.

In the 800 rpm weld, periodically spaced bands enriched in W were observed in the stir zone that provided a clear marker of the tool / workpiece interface during welding. The formation of the bands was attributed to diffusion tool wear induced by large thermal gradients created in the stir zone by the low thermal conductivity of the workpiece compared to the tool.

Acknowledgements

This work was supported by the NSF-I/UCRC, Center for Friction Stir Processing, Grant # EEC-0437341. Two of the authors (ALP and JCW) would like to acknowledge funding from the Office of Naval Research (contract: N00014-06-1-0089). ALP also acknowledges the encouragement of the Air Force Research Laboratory management and support from Air Force Contract FA8650-07-D-5800 during the preparation of this manuscript.

References

1. W.M. Thomas, E.D. Nicholas, J.C. Needham, M.G. Church, P. Templesmith, C.J. Dawes: International Patent Application No. PCT/GB92/02203.

2. W.D. Lockwood, B. Tomaz, A.P. Reynolds: Materials Science and Engineering A, 2002. 323: pp. 348-353.

3. C.G. Rhodes, M.W. Mahoney, W.H. Bingel, R.A. Spurling and C.C. Bampton: Scripta Materialia, 36(1), 1997, pp. 69-75.

4. W.B. Lee, Y.M. Yeon and S.B. Jung: Scripta Materialia, 49, 2003, pp. 423-428.

5. R.S. Mishra and Z.Y. Ma: Materials Science and Engineering R, 50, 2005, pp.1-78.

6. J. Schneider, R. Beshears and A.C. Nunes Jr.: Interfacial sticking and slipping in the friction stir welding process, Materials Science and Engineering A, 435-436 (2006) pp. 294-304.

7. T. U. Seidel and A. P. Reynolds: *Metall. Mater. Trans. A*, 32A, 2001, pp. 2879-2884.

8. A.L. Pilchak, M.C. Juhas and J.C. Williams: Metallurgical and Materials Transactions, 38A, 2007, pp. 401-408.

9. D.P. Field, T.W. Nelson, Y. Hovanski, and K.V. Jata: Metall. Mater. Trans. A, 32;11, 2001, pp. 2869-2877.

10. R.W. Fonda, J.F. Bingert and K.J. Colligan: Scripta Materialia, 51, 2004, pp. 243-248.

11. R.W. Fonda, J.A. Wert, A.P. Reynolds and W. Tang: Friction stir welding of single crystal aluminum, Science and Technology of Welding and Joining, 12;4 (2007) p. 304-310.

12. A.P. Reynolds, E. Hood and W. Tang: Scripta Materialia, 52, 2005, pp. 491-494.

13. K.E. Knipling and R.W. Fonda: Scripta Materialia, 60, 2009, pp. 1097-1100.

14. A.L. Pilchak, PhD Dissertation, The Ohio State University, 2009.

15. J.-H. Cho, D.E. Boyce and P.R. Dawson: Materials Science and Engineering A, 398, 2005, -pp. 146-163.

16. J.-H. Cho and P.R. Dawson: Metallurgical and Materials Transactions A, 37 (2006) p. 1147-1164.

17. M.M.Z. Ahmed, B.P. Wynne, W.M. Rainforth and P.L. Threadgill: Scripta Materialia, 59, 2008, p. 507-510.

18. S. Mironov, Y. Zhang, Y.S. Sato and H. Kokawa: Scripta Materialia, 59 (2008) p. 511-514.

19. M.C. Juhas, G.B. Viswanathan, H.L. Fraser, in: Proceedings of the Second Symposium on Friction Stir Welding, Gothenburg, Sweden, June 2000 (CD proc.).

20. T.J. Lienert, K.V. Jata, R. Wheeler, V. Seetharaman, in: Proceedings of the Joining of Advanced and Specialty Materials III, ASM International, Materials Park, OH, USA, 2001, pp. 160-167.

21. A.J. Ramirez and M.C. Juhas: Materials Science Forum, 426-432, 2003, pp. 2999-3004.

22. Y. Zhang, Y.S. Sato, H. Kokawa, S.H.C. Park and S. Hirano: Materials Science and Engineering A, 2008, pp. 448-455.

23. L. Zhou, H.J. Liu and Q.W. Liu: J. Mater. Sci., 45, 2010, pp. 39-45.

24. S. Mironov, Y. Zhang, Y.S. Sato and H. Kokawa: Scripta Materialia, 59, 2008, p. 27-30.

25. S.C. Wang, M. Aindow and M.J. Starink: Acta Materialia, 51, 2003, pp. 2485-2503.

26. N. Karogal: Masters Thesis, The Ohio State University, Department of Welding Engineering, 2002.

27. A.L. Pilchak, Z.T. Li, J.J. Fisher, A.P. Reynolds, M.C. Juhas and J.C. Williams: *in* Friction Stir Welding and Processing IV, R.S. Mishra, M.W. Mahoney, T.J. Lienert, and K.V. Jata, eds., TMS, Warrendale, PA, 2007, pp. 419-427.

28. C. Leyens and M. Peters: Titanium and Titanium Alloys, Wiley-VCH, Cologne, 2003, pp. 1-34.

29. W.B. Lee C.Y. Lee, W.S. Chang, Y.M. Yeon and S.B. Jung: Materials Letters, 59, 2005, pp. 3315-3318.

30. A.L. Pilchak, M.C. Juhas and J.C. Williams: Metall. Mater. Trans. A, 38, 2007, p. 435-437.

31. A.L. Pilchak, M.C. Juhas and J.C. Williams: *in* IIW-3 Conf. Proc., Welding in the World, Dubrovnik, Croatia. Vol. 52, nº 9/10 (2008) – Research Supplement.

32. M. Boivineau, C. Cagran, D.E. Doytier, V. Eyraud, M.-H. Nadal, B. Wilthan and G. Pottlacher: International Journal of Thermophysics, 27(2), 2006, pp. 507-529.

33. J.C. Williams, R.G. Baggerly and N.E. Paton: Metallurgical and Materials Transactions A, 33, 2002, pp. 837-850.

34. M.G. Glavicic, P.A. Kobryn, T.R. Bieler and S.L. Semiatin: Materials Science and Engineering A, 346 (2003) p. 50-59.

35. M.G. Glavicic, P.A. Kobryn, T.R. Bieler and S.L. Semiatin: Materials Science and Engineering A, 351, 2003, pp. 258-264.

36. W.G. Burgers: Physica, 1, 1934, pp. 561-586.

37. A.L. Pilchak and J.C. Williams, submitted to Met. Trans. A. (09/27/2009), manuscript: E-TP-09-812-A

38. C. Cayron: Acta Crystallographica Section A Foundations of Crystallography, A62, 2006, pp. 21-40.

39. G. Lütjering and J.C. Williams: *Titanium*, Springer-Verlag, New York, NY, 2003.

40. T. Long, W. Tang and A.P. Reynolds: Science and Technology of Welding and Joining, 12(4), 2007, pp. 311-317.

41. ASM Metals Handbook, 10th ed., Vol. 2. Properties and Selection of Non-ferrous Alloys and Special Purpose Materials, ASM International, 1990, pg. 562.

42. Y.J. Chao, X. Oi and W. Tang: Journal of Manufacturing Science and Engineering – Transactions of the ASME, 125(1), 2003, pp. 138-145.

43. G. Lütjering: Materials Science and Engineering A, 243, 1998, pp.32-45.

44. T.R. Bieler and S.L. Semiatin: International Journal of Plasticity, 18, 2002, pp. 1165-1189.

45. L. Germain, N. Gey, M. Humbert, P. Bocher and M. Jahazi: Acta Materialia, 53, 2005, pp. 3535-3543.

46. M. Peters, A. Gysler and G. Lütjering: *in* Titanium '80 Science and Technology, Proceedings of the Fourth International Conference on Titanium, H. Kimura and O. Izumi, eds., Kyoto, Japan, (1980) p. 1777-1786.

47. M. Hölscher, D. Raabe and K. Lücke, Steel Research, 62:12, 1991, p. 567-575.

48. U.F. Kocks, C.N. Tomé and H.-R. Wenk: Texture and Anisotropy: Preferred Orientations in Polycrystals and their Effect on Materials Properties, Cambridge University Press, New York, NY, 1998.

49. D. Bhattacharyya, G.B. Viswanathan, S.C. Vogel, D.J. Williams, V. Venkatesh and H.L. Fraser: Scripta Materialia, 54, 2006, pp. 231-236.

50. J. Baczynski and J.J. Jonas: Acta Materialia, 44;11, 1996, pp. 4273-4288.

51. S. Li, I.J. Beyerlein and M.A.M. Bourke: Materials Science and Engineering A, 493, 2005, pp. 66-77.

52. N. Stanford and P.S. Bate: Acta Materialia, 52, 2004, pp. 5215-5224.

53. L. Zeng and T.R. Bieler: Materials Science and Engineering A, 392, 2005, pp. 403-414.

54. M.W. Mahoney, C.G. Rhodes, J.G. Flintoff, R.A. Spurling and W.H. Bingel: Metall. Mater. Trans. A, 29(7), 1998, pp. 1955-1964.

55. R.W. Fonda and J.F. Bingert: Scripta Materialia, 57, 2007, pp. 1052-1055.

56. Landolt-Börnstein - Group IV Physical Chemistry: Ti-W phase diagram, *in* Volume 5, Springer-Verlag, p.1-2, 1998.

57. S. Zhang, J.F. Li, J.X. Deng and Y.S. Li: Int. J. Adv. Manuf. Technol., 44, 2009, pp. 17-25.

Tables:

Table I. Welding parameters utilized in the present study. All welds were made in 10.3 mm thick plate with a tool back tilt of 1°. The first number in the weld ID corresponds to the tool travel speed in inches min^{-1}.

Weld ID	RPM	Welding Speed mm min^{-1}
2-120	120	50.8
2-150	150	50.8
2-200	200	50.8
4-400	400	101.6
8-800	800	203.2

Figures and figure captions:

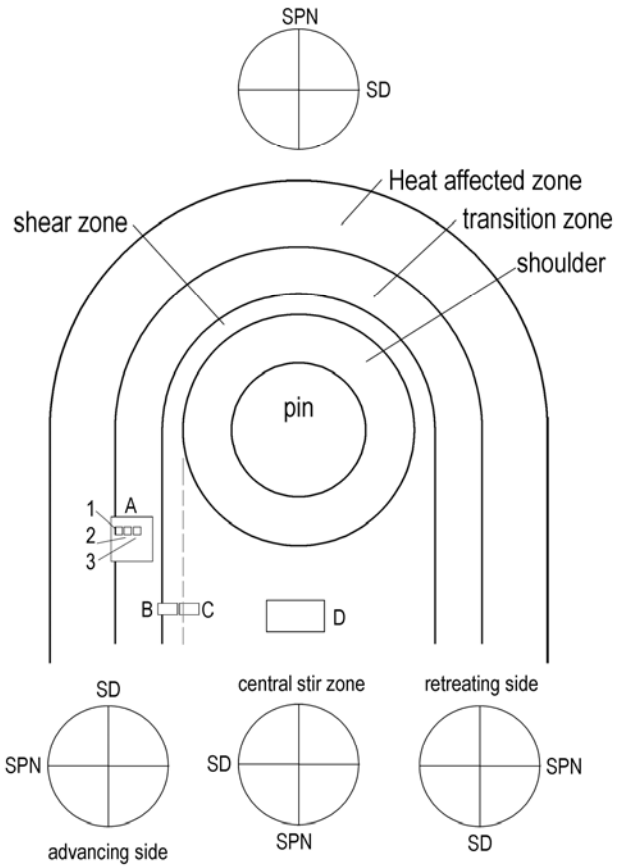

Figure 1. Schematic representation of the various microstructure regions around the friction stir tool [8]. Letters A through D designate the location where EBSD scans were acquired at the midplane of the stir zone. The tool is traveling up, rotating clockwise about the axis perpendicular to the plane of the page (neglecting back tilt). The orientation of the presumed shear plane normal (SPN) and shear direction (SD) is shown at four locations around the tool.

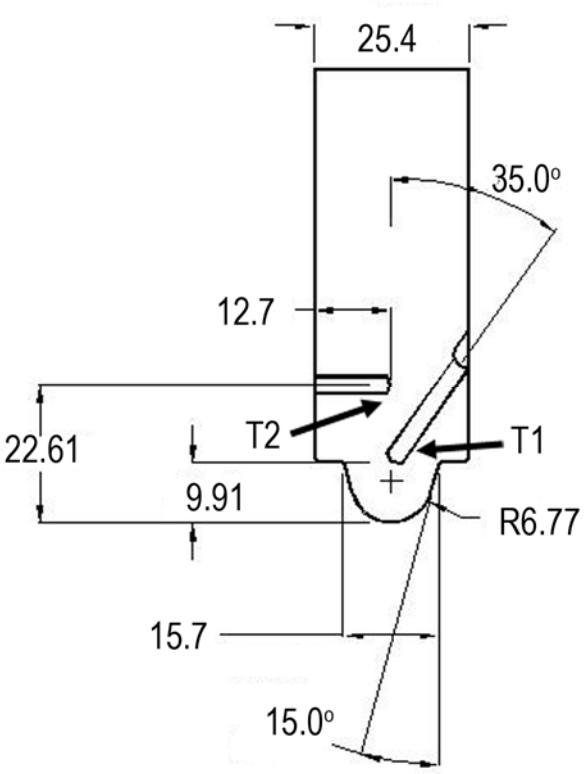

Figure 2. Tool geometry used in the present study.

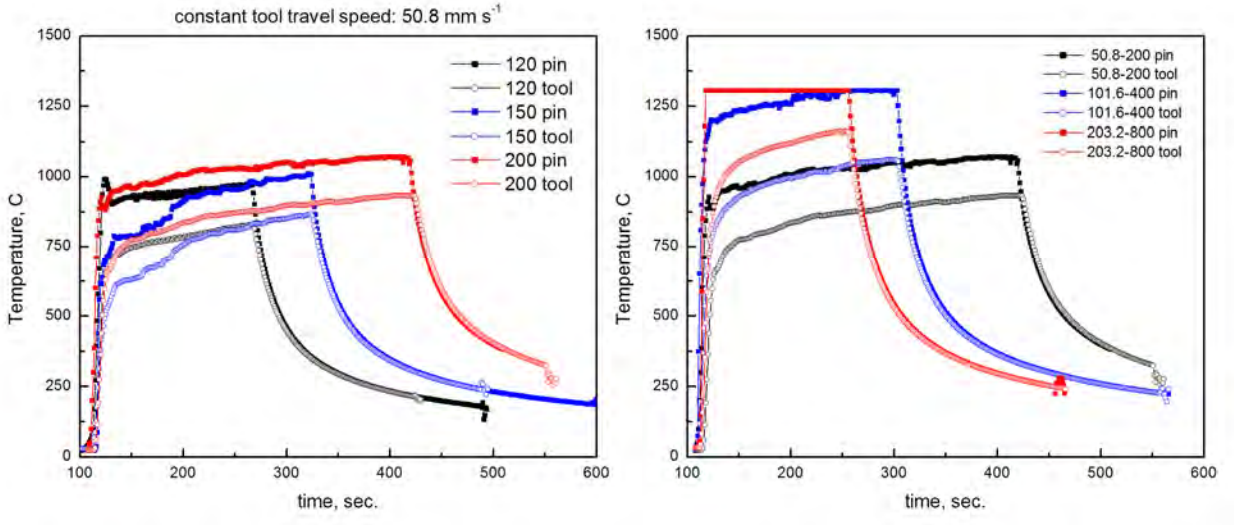

Figure 3. In tool temperature measurements from the 120, 150, 200, 400 and 800 rpm welds; the T1 temperature exceeded the thermocouple limit in the 800 weld and near the end of the 400 rpm weld.

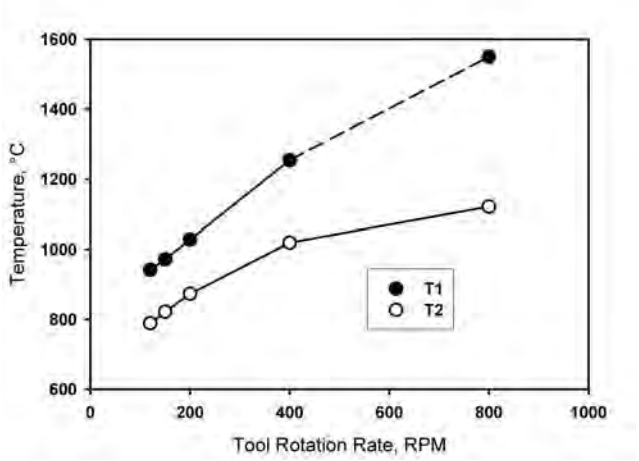

Figure 4. Maximum tool temperature vs. rotational speed. The dashed line indicates that this value was calculated as discussed further in the text.

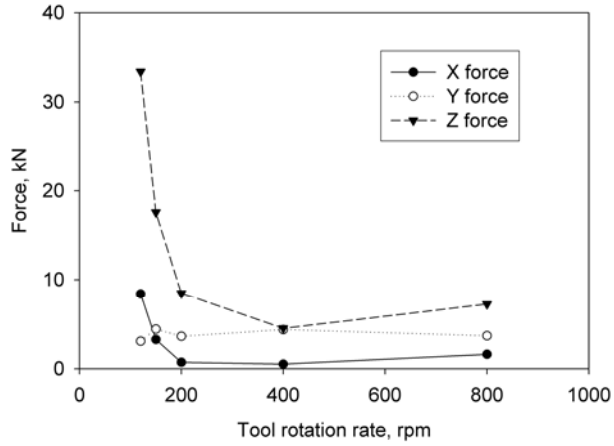

Figure 5. Welding forces as a function of tool rotation speed.

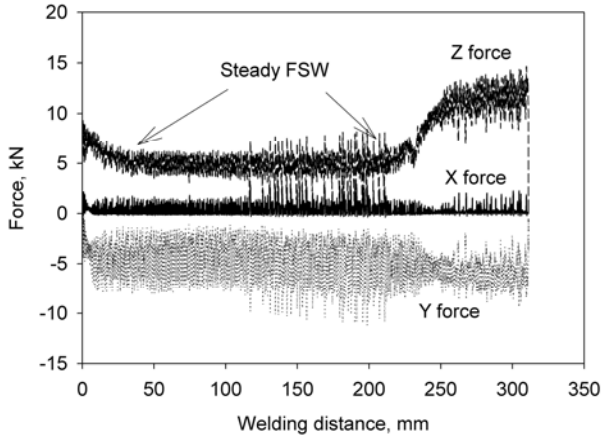

Figure 6. Forces on the welding tool for the 4-400 weld.

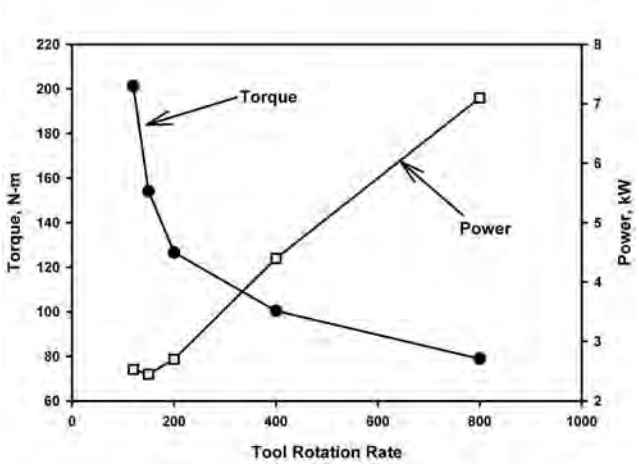

Figure 7. Torque and power feedback as a function of tool rotation speed.

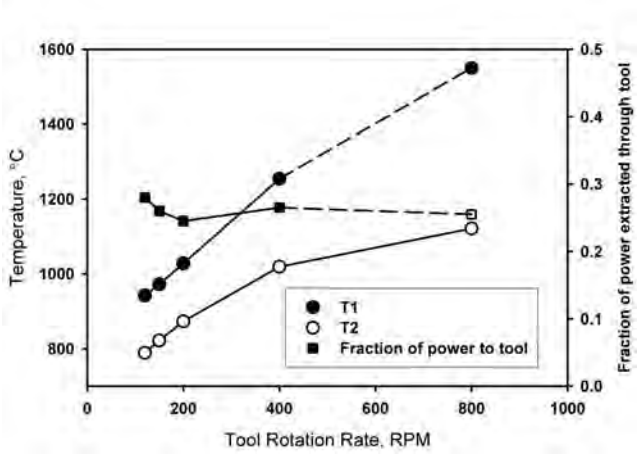

Figure 8. Heat flux and peak tool temperature as a function of tool rotation speed.

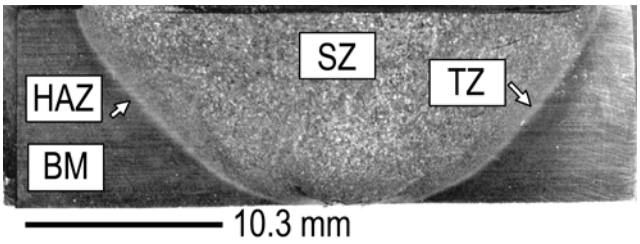

Figure 9. Macroscopic cross section of the 800 rpm weld with the four characteristic regions [8] of the weld indicated.

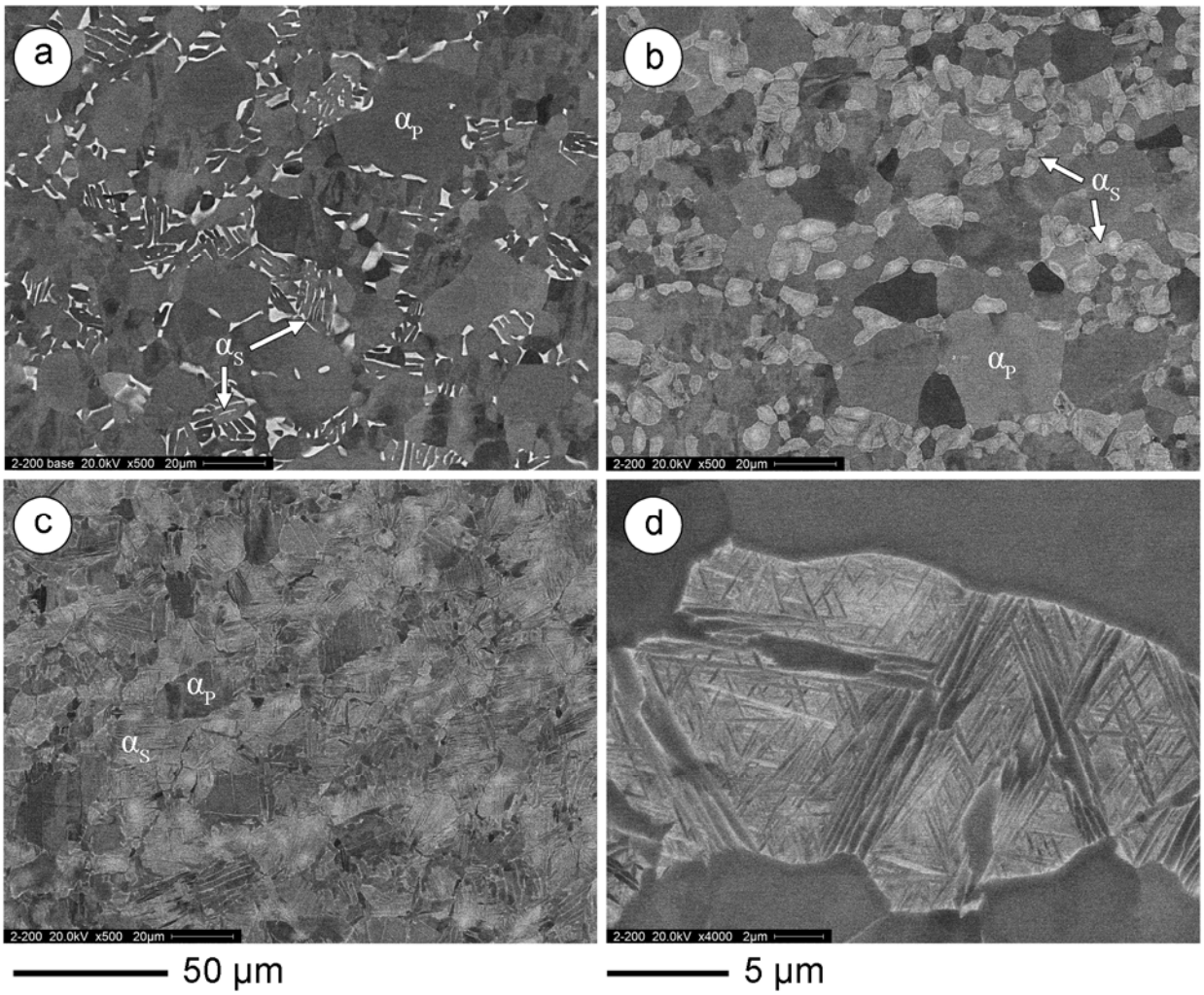

Figure 10. Backscattered SEM images at the same magnification of the (a) base metal, (b) heat affected zone, and (c) transition zone microstructures of the 200 rpm weld showing the fine scale of the α precipitates. (d) Higher magnification of the decomposed β phase regions in the heat affected zone.

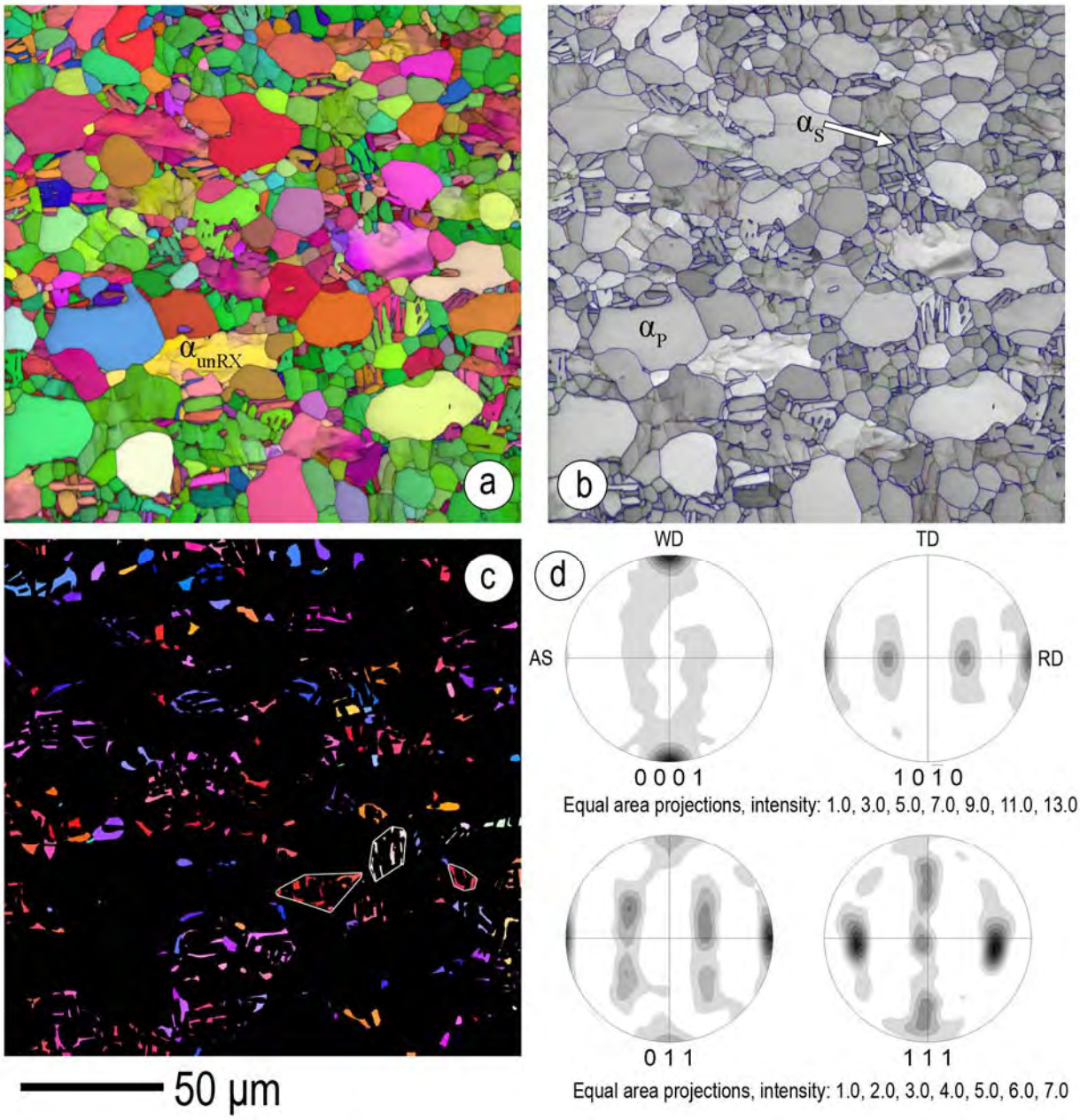

Figure 11. (a) Normal direction (tool rotation axis) inverse pole figure crystal orientation map, shaded with greyscale according to the image quality parameter, of the base material showing both the α and β phases, (b) greyscale image quality parameter map with boundaries between adjacent grains colored according to their misorientation angle: $2^o \leq$ red $< 5^o$, $5^o \leq$ green $< 15^o$, blue $\geq 15^o$, (c) normal direction (tool rotation axis) inverse pole figure crystal orientation map of the β phase only, and (d) texture of the α and β phase in the base material.

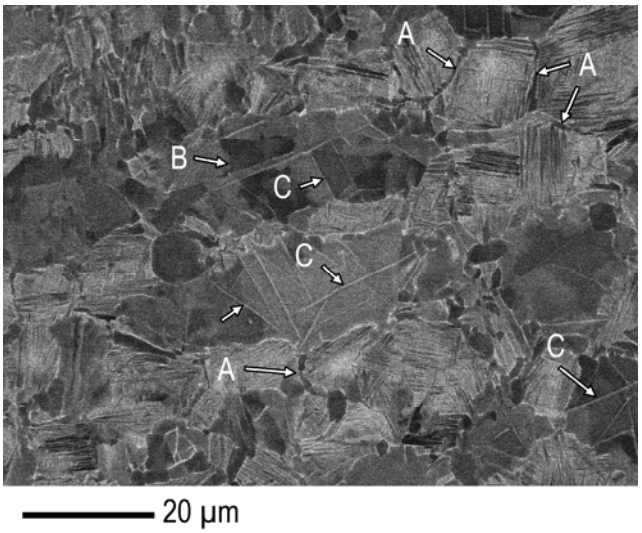

Figure 12. Backscattered electron image of the transition zone, very near to the shear zone, showing the formation of (A) grain boundary α in the transition zone along with orientation contrast (B) and slip traces (C) within the globular α.

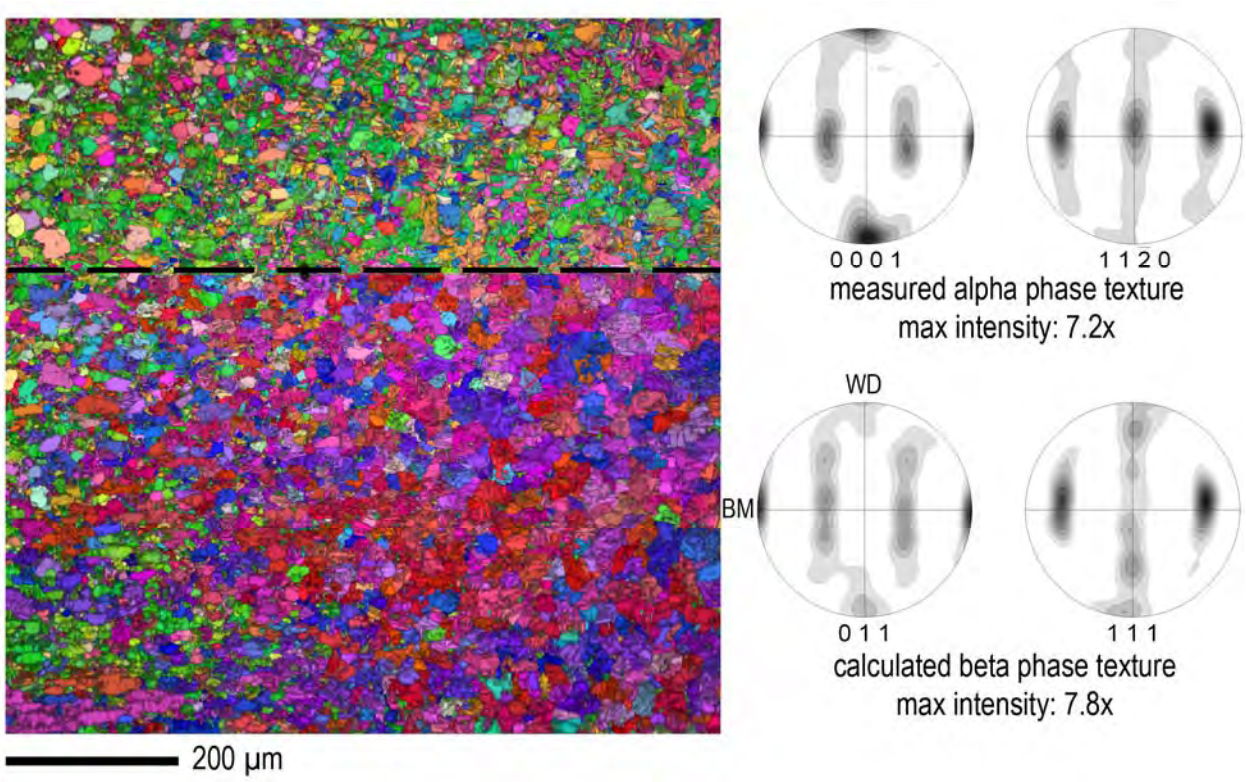

Figure 13. Combined α and β normal direction colored IPF map of the transition zone. Only the section of the data beneath the horizontal dashed line was reconstructed. The grains with green and orange hues in the lower portion of the image on the left side are equiaxed α phase that was not transformed during reconstruction. The α and β phase texture for the α and reconstructed β grains in this region are shown on equal area projections with intensity increments of 1.0x each.

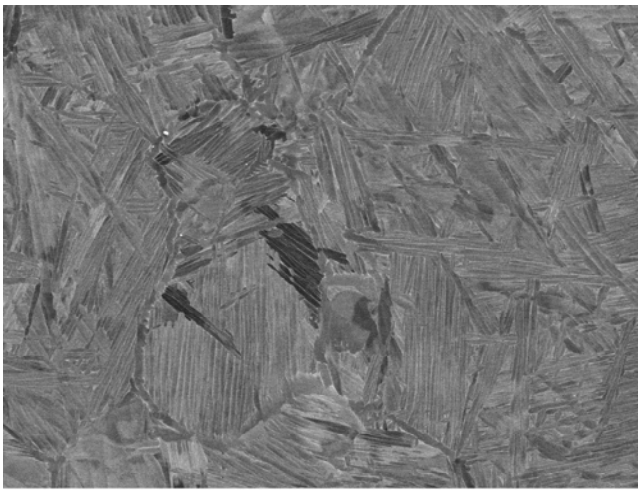

Figure 14. Backscattered electron image of the central stir zone microstructure in the 200 rpm weld.

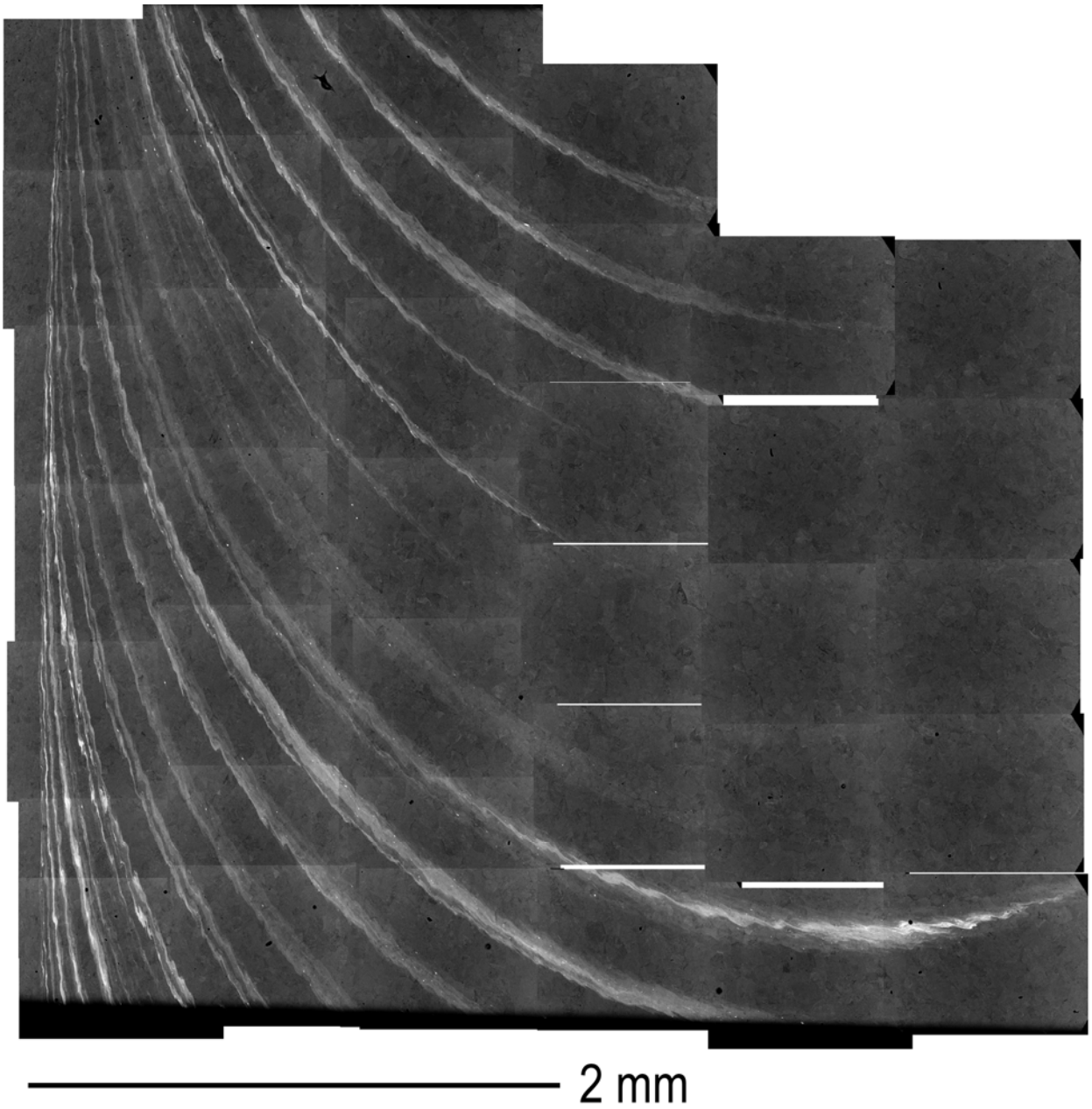

Figure 15. Backscattered electron image montage of part of the stir zone interface in the 800 rpm weld in plan view. The bright bands contain tungsten tool material in solid solution.

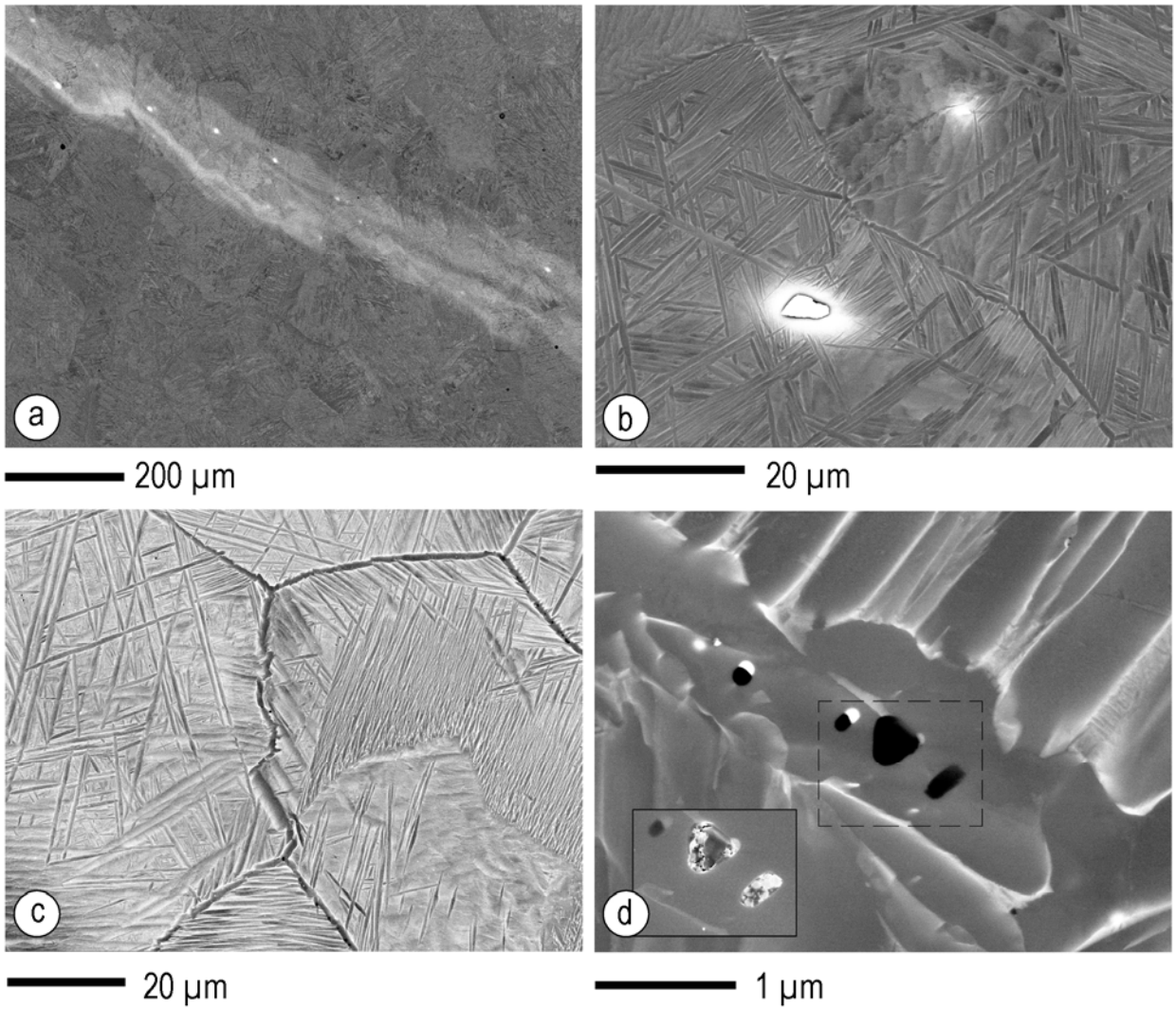

Figure 16. Higher magnification images of the tungsten-rich bands in the stir zone of the 800 rpm weld. See text for additional details.

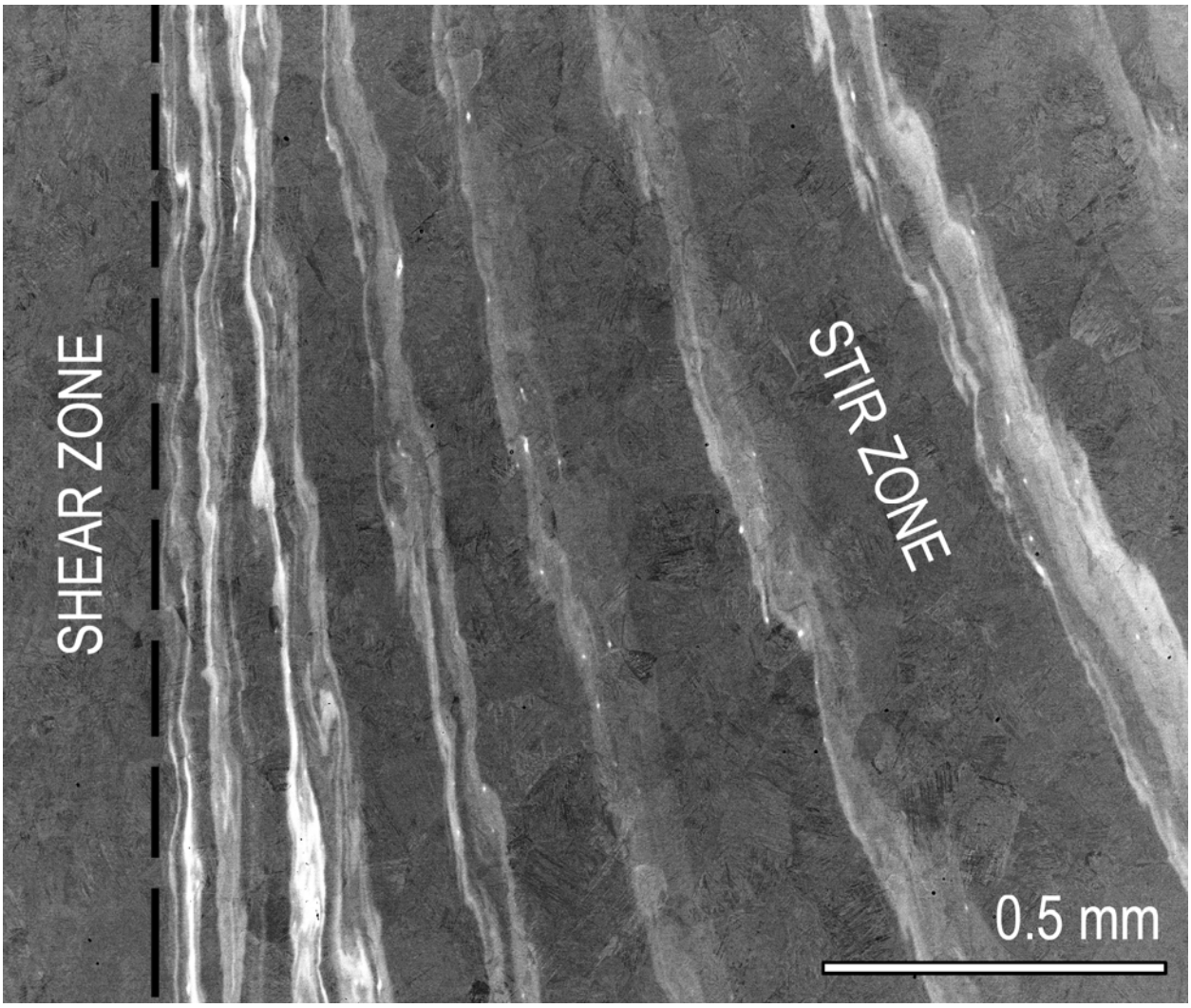

Figure 17. Backscattered electron image showing the interface between the shear zone and stir zone in the 800 rpm weld as indicated by the W-rich bands.

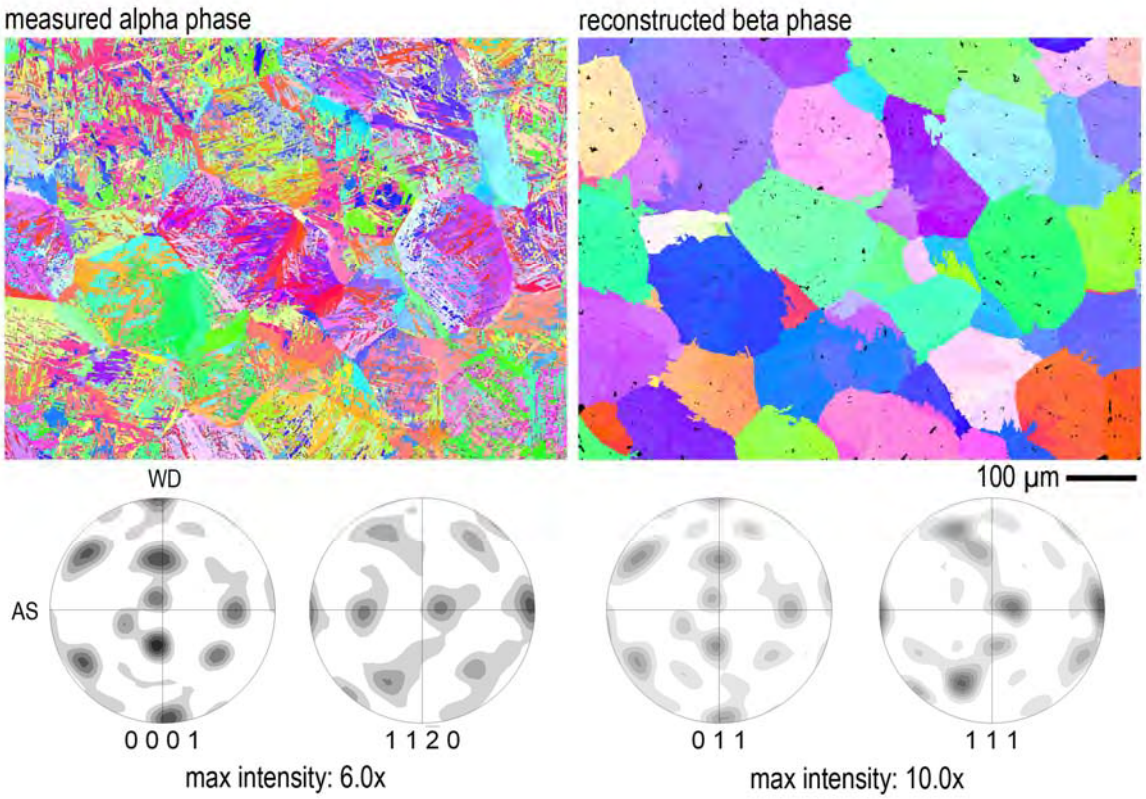

Figure 18. Tool rotation axis inverse pole figure maps and pole figures of the α and reconstructed β phases and pole figures from the central stir zone (location D) of the 800 rpm weld. The intensity levels are in increments of 1.0x and 2.0x random for the α and β phase, respectively.

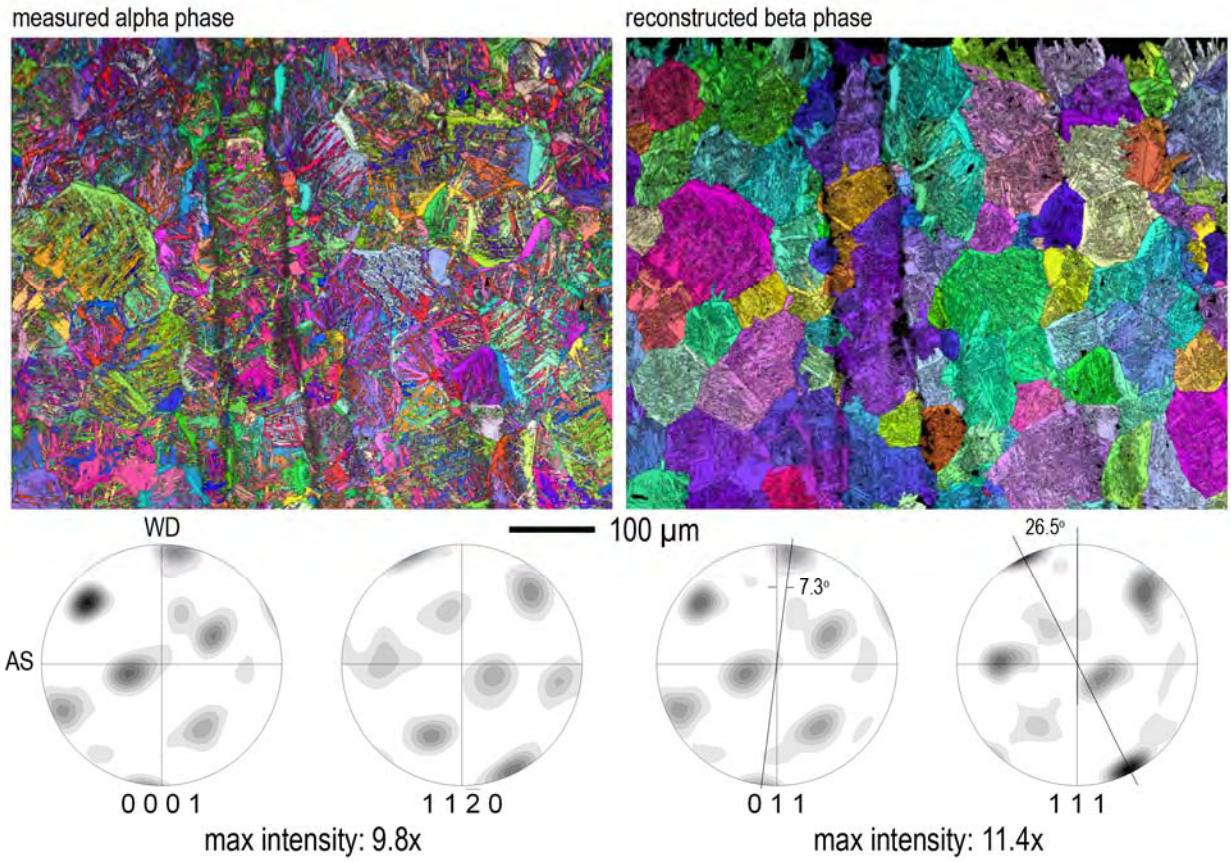

Figure 19. Tool rotation axis inverse pole figure maps and pole figures of the α and reconstructed β phases and pole figures from the advancing side (location C) of the 800 rpm weld.

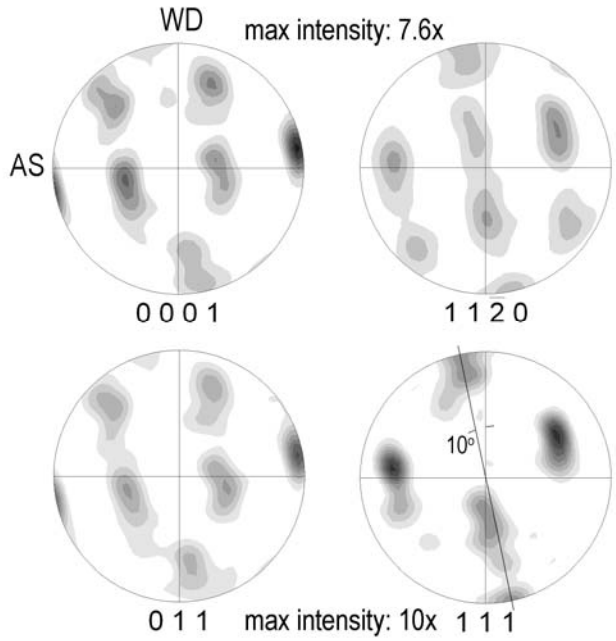

Figure 20. Measured α and reconstructed β phase texture in the shear zone (location B). The intensity levels are in increments of 1.0x random.

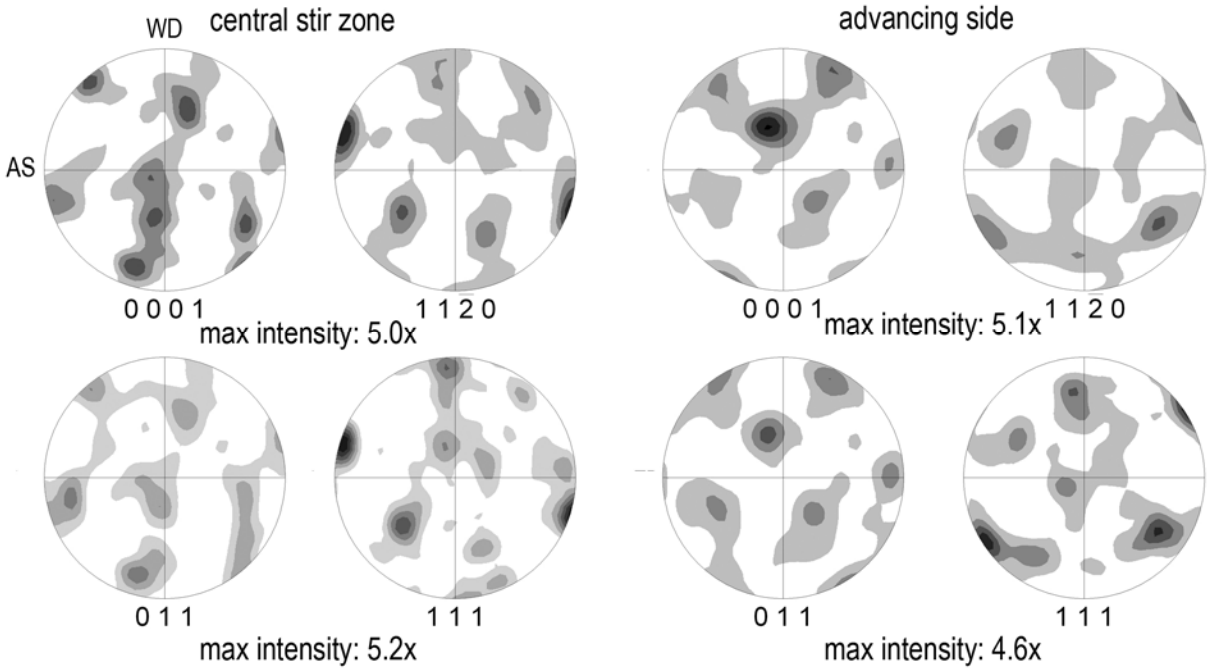

Figure 21. Measured α phase and reconstructed β phase textures from the central stir zone and advancing side for the 200 rpm weld. The intensity levels are in increments of 1.0x random.

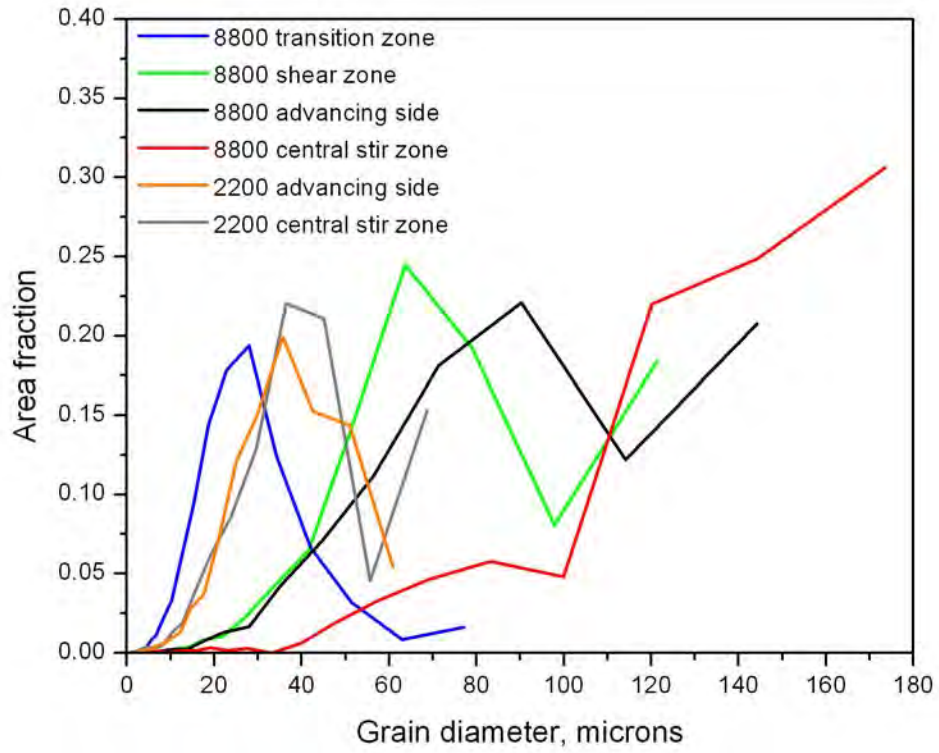

Figure 22. Calculated prior β grain size distributions from various regions of the 200 and 800 rpm welds.